Chapter 6

Reduction in Dimensionality

6.1 Introduction

The moving force identification algorithm outlined in the previous chapter requires the use of the full system matrices for the dynamic programming routine. Whilst this is acceptable for small finite element models, for larger models where the number of nodes will generally exceed 1000 the storage requirements and the computational time are very expensive, and the implementation of the moving force identification algorithm is not really feasible. There are currently two methods to reduce the order of the system outlined in chapter 2. The first is the Chandrasekhar recursions (Trujillo & Busby 1997, Kailath 1972, Morf et al 1974, Adams & Doyle 2002, Doyle 2004, Park et al 1993) which rely on the symmetric property of the R_n's to derive an incremental formula for the change in R between two successive time steps. However, the Chandrasekhar recursions require that the system matrices [K] and [T] remain constant over all time steps, so this method is not applicable to the MFI problem. Later Sayed & Kailath (1994) extended the Chandrasekhar recursions to a structured class of linear time variant systems; unfortunately it was found that this class of structure is not applicable to the moving force identification algorithm. The alternative method, which is applicable to this problem, is the eigenvalue reduction technique (Busby & Trujillo 1996, Trujillo & Busby (1997).

The following sections outline the theory of the eigenvalue reduction technique and its application to a two-span continuous bridge. The eigenvalue reduction technique is then compared to the moving force identification algorithm using the full system matrices for the vehicle bridge interaction model outlined in section (4.7). The eigenvalue reduction technique is further improved by changing the assumption made in chapter 4 that if a force is located between nodes, one can regularised as if the force is located at the closet node. The new assumption is that if a force is located between the nodes of an element, the regularised force is distributed to the degrees of freedom as a product of the shape functions. Finally an error analysis is carried out on the moving force identification algorithm.

6.2 Eigenvalue Reduction

The equation of motion for an undamped system in free vibration can be written as,

$$[M_g]\{\ddot{y}\} + [K_g]\{y\} = 0 \tag{6.1}$$

It is assumed that the solution to equation (5.1) is of the form, (Bathe 1982),

$$y(t) = \phi \sin(\omega(t - t_0)) \tag{6.2}$$

Where ϕ is a vector of order n_{dof} corresponding to the number of degrees of freedom in the model, t_0 is the phase angle and ω is the constant identified to represent natural frequency. Substituting equation (6.2) into (6.1) results in the standard characteristic equation (Craig 1981, Clough & Penzien 1975),

$$[K_g] - \omega^2[M_g] = 0 \tag{6.3}$$

The eigenvalues or the squared natural frequencies ω_n^2 can be found by solving the polynomial equation of degree *n*, resulting from the expansion of the determinant of equation (5.3). The eigenvalues can then be ordered from lowest to highest,

$$0 \le \omega_1^2 \le \omega_2^2 \ldots \le \omega_n^2 \tag{6.4}$$

Corresponding to each eigenvalue there will be an eigenvector ϕ or natural mode shape. If an eigenvalue analysis is performed on equation (6.3), each eigenvalue ω_i^2 has a corresponding eigenvector ϕ_i that satisfies the following relationship,

$$[K_g]\phi_i = \omega_i^2[M_g]\phi_i, i = 1, 2 \ldots n \tag{6.5}$$

Each eigenvector is normalised with respect to $[M_g]$ and $[K_g]$ and the resulting relationships are,

$$\phi_i^T[M_g]\phi_i = 1 \tag{6.6}$$

$$\phi_i^T [K_g] \phi_i = \omega_i^2 \tag{6.7}$$

With the above definitions the following orthogonal conditions are satisfied,

$$\phi_i^T [M_g] \phi_j = 0, i \neq j \tag{6.8}$$

$$\phi_i^T [K_g] \phi_j = 0, i \neq j \tag{6.9}$$

the eigenvectors can then be combined into a single matrix,

$$\Phi = [\phi_1, \phi_2, \phi_3, ... \phi_n] \tag{6.10}$$

Substituting equation (6.10) into equations (6.6) and (6.7) gives

$$\Phi^T [M_g] \Phi = \begin{bmatrix} 1 & 0 & 0 & 0 \\ 0 & 1 & 0 & 0 \\ 0 & 0 & . & . \\ 0 & 0 & . & 1 \end{bmatrix} = [I] \tag{6.11}$$

$$\Phi^T [K_g] \Phi = \begin{bmatrix} \omega_1^2 & 0 & 0 & 0 \\ 0 & \omega_2^2 & 0 & 0 \\ 0 & 0 & . & . \\ 0 & 0 & . & \omega_n^2 \end{bmatrix} = [\Omega] \tag{6.12}$$

It is assumed that the vector of displacements can be replaced with an equivalent system of the form,

$$\{y\}_{n_{dof} x 1} = [\Phi]_{n_{dof} x n_z} \{z\}_{n_z x 1} \tag{6.13}$$

Where n_n is the number of modes used in the analysis, substituting equation (6.13) into equation (4.32) gives

$$[M_g][\Phi]\{\ddot{z}\} + [C_g][\Phi]\{\dot{z}\} + [K_g][\Phi]\{z\} = [L(t)]\{g(t)\} \tag{6.14}$$

The decoupled equations of motion can be derived if it is assumed that the damping matrix $[C_g]$ conforms to the orthogonal conditions defined by

$$\phi_i^T [C_g] \phi_j = 0 \tag{6.15}$$

$$\phi_i^T [C_g] \phi_i = 2\xi_i \omega_i \tag{6.16}$$

Where i is the i^{th} mode and ξ_i is the modal damping ratio of the i^{th} mode. The damping effects can be taken into account if Raleigh damping, (Bathe 1982, Clough & Penzien 1975) is assumed. Raleigh damping assumes that the damping matrix $[C_g]$ can be defined as a linear combination of the stiffness and mass matrices,

$$[C_g] = \alpha [M_g] + \beta [K_g] \tag{6.17}$$

where α and β are constants that are to be determined from two given damping ratios corresponding to two different frequencies (Bathe 1982). Substituting equation (6.17) into (6.16) gives,

$$\phi_i^T (\alpha [M_g] + \beta [K_g]) \phi_i = 2\xi_i \omega_i \tag{6.18}$$

$$\alpha \phi_i^T [M_g] \phi_i + \beta \phi_i^T [K_g] \phi_i \tag{6.19}$$

$$\alpha + \beta \omega_i^2 = 2\omega_i \xi_i \tag{6.20}$$

Premultiplying equation (6.14) by $[\Phi]^T$ gives,

$$[\Phi]^T [M_g] [\Phi] \{\ddot{z}\} + [\Phi]^T [C_g] [\Phi] \{\dot{z}\} + [\Phi]^T [K_g] [\Phi] \{z\} = [\Phi]^T [L(t)] \{g(t)\} \tag{6.21}$$

$$[I] \{\ddot{z}\} + 2\xi [\Omega] \{\dot{z}\} + [\Omega] \{z\} = [\Phi]^T [L] \{g(t)\} \tag{6.22}$$

Equation (6.22) is converted to a vector matrix differential equation as outlined in section 2.2:

$$\frac{d}{dt}\begin{Bmatrix} z \\ \dot{z} \end{Bmatrix} = \begin{bmatrix} 0 & I \\ -\Omega & -2\xi\Omega \end{bmatrix}\begin{Bmatrix} z \\ \dot{z} \end{Bmatrix} + \begin{bmatrix} 0 \\ \Phi^T[L(t)] \end{bmatrix}\{g(t)\} \tag{6.23}$$

$$\left(\frac{dX}{dt}\right) = [A]\{X\} + f(t) \tag{6.24}$$

Using the method outlined in section 4.4.1, equation (6.23) can be converted into first order system suitable for dynamic of the form,

$$\begin{Bmatrix} X \\ g \end{Bmatrix}_{j+1} = [K^*]_j \begin{Bmatrix} X \\ g \end{Bmatrix}_j + [T^*]\{r\} \tag{6.25}$$

where $[K^*]$ and $[T^*]$ are the system matrices derived using the decoupled equations of motion. As the state variables have been changed, the relationship between the measurements and the state variables must also be modified. This relationship can be defined by,

$$\{\varepsilon\}_j = Q\begin{pmatrix} \Phi & 0 & 0 \\ 0 & \Phi & 0 \\ 0 & 0 & 0 \end{pmatrix}\begin{Bmatrix} X_j \\ g_j \end{Bmatrix} \tag{6.26}$$

where $[Q]$ is the selector matrix for the finite element model. With these definitions the dynamic programming routine for the first order regularisation of moving forces as outlined in chapter 4, can be implemented with a significant reduction in the storage required.

6.3 Two-Span Continuous Bridge Model and Dynamic Simulation

A two-span continuous bridge with two 40m spans is modelled using the finite element method, see figure 6.1. The bridge model has a cross-sectional area A, of 14.3 m^2 and second moment of area I, of 1.923 m^4, the depth of the bridge is 2m with the neutral axis y located at 0.97 m from the top, see figure 6.2. It has a Modulus of Elasticity E, of 3.5 x 10^{10} N/m^2 and density ρ, of 2400 kg/m^3. The bridge is discretised into 160 equal beam elements with two degrees of freedom per node, a rotation and a translation.

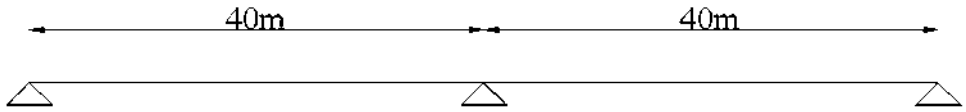

Figure 6.1 – Two-span continuous bridge model

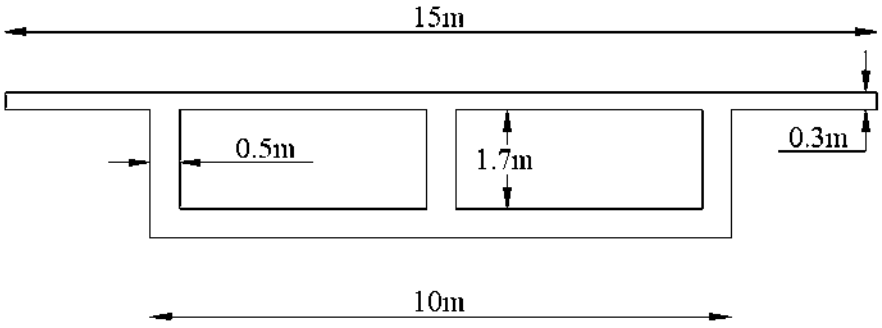

Figure 6.2 – Cross –section of two span continuous bridge model

6.3.1 Free Vibration at the Second Natural Frequency Due to Vehicle Velocity

During the course of this study it was observed that the velocity of the moving forces can affect the mode at which the structure vibrates after the forces have traversed the bridge. The first two natural frequencies of the finite element model are 1.37 Hz and 2.147 Hz see figures 6.3 and 6.4. Normally after the forces have crossed the bridge the free vibration would occur at the first natural frequency, however it was observed that certain velocities cause the structure to vibrate at its second natural frequency after the forces have crossed the bridge. The translation of the bridge at 20 m and 60 m is simulated due to the passage of a constant load of 100,000 N with a velocity of 22 m/s using the method of simulation outlined in section 4.2. From figure 6.5 it can be seen that when the force has traversed the bridge, the structure is vibrating at its second natural frequency. In order to show that the vibration at the second natural frequency is velocity dependent, two moving constant forces of 100,000 N were simulated with an axle spacing of 2 m travelling at 22 m/s. From figure 6.6 it can be seen that the bridge will still vibrate at its second natural frequency due to the velocity.

In total four velocities were found using a parametric study of velocity, which could potentially cause the structure to vibrate at its second natural frequency after the forces have traversed the bridge. These are 8.46 m/s, 22 m/s, 36.7 m/s and 55 m/s. Figure 6.7 shows the translation at 20 and 60 m due to a force of 100000 N crossing the bridge at 8.46 m/s, again it can be seen that the free vibration of the bridge occurs at the second natural frequency of 2.147 Hz.

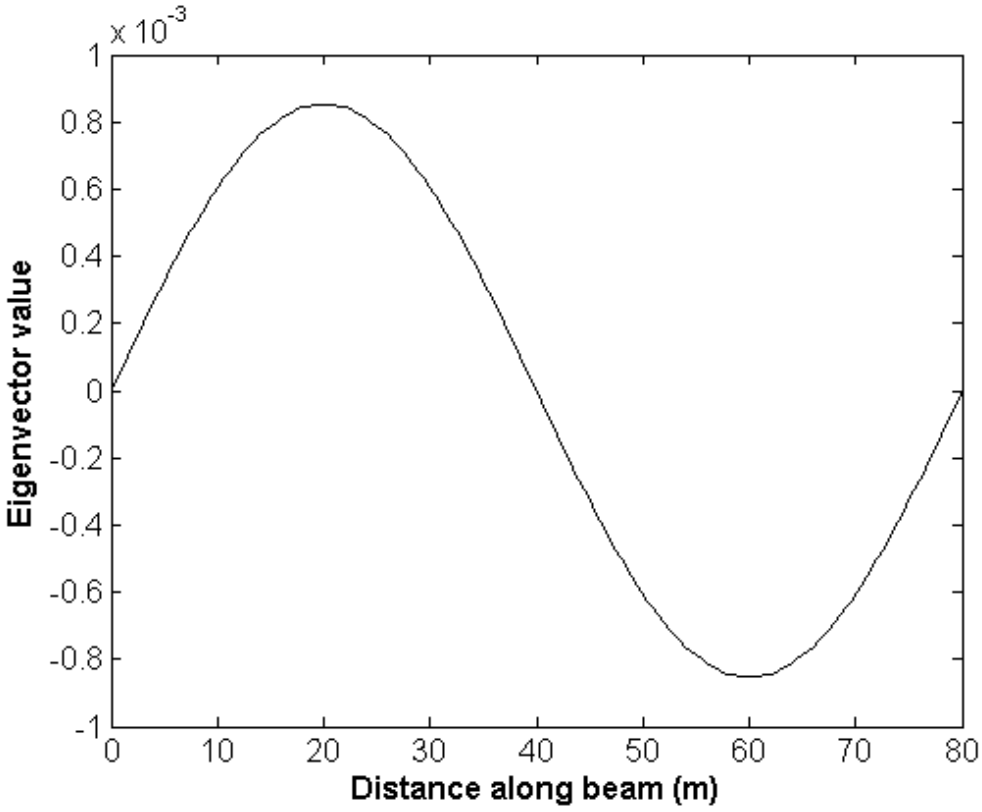

Figure 6.3 – Mode shape of the first natural frequency 1.47 Hz

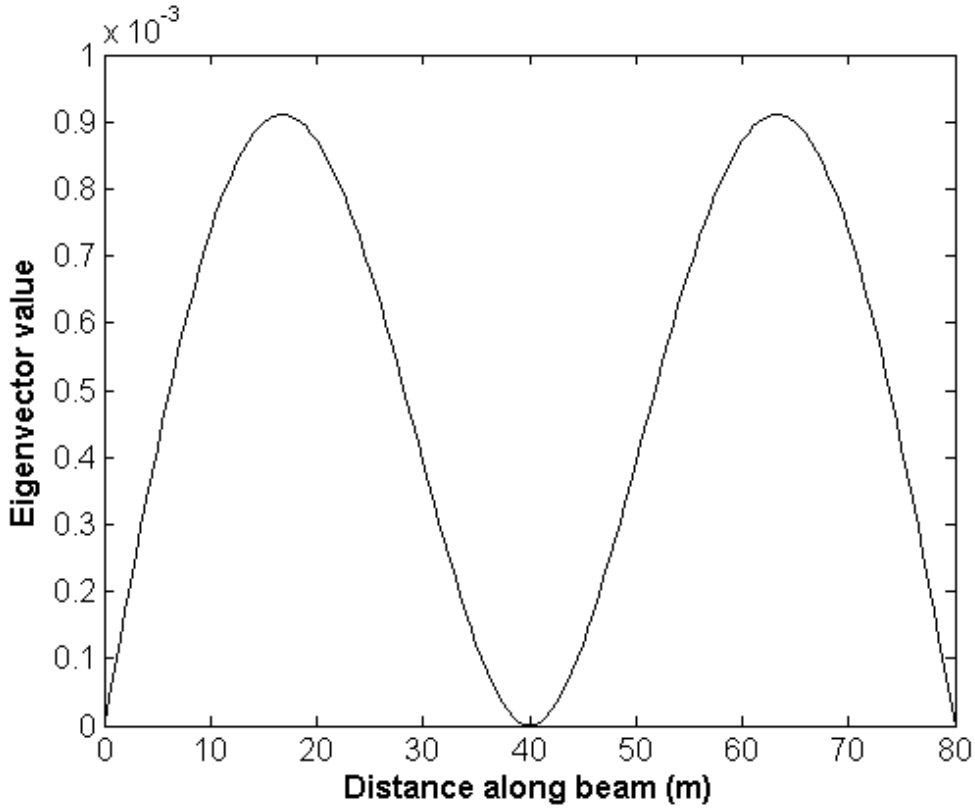

Figure 6.4 – Mode shape of the second natural frequency 2.147 Hz

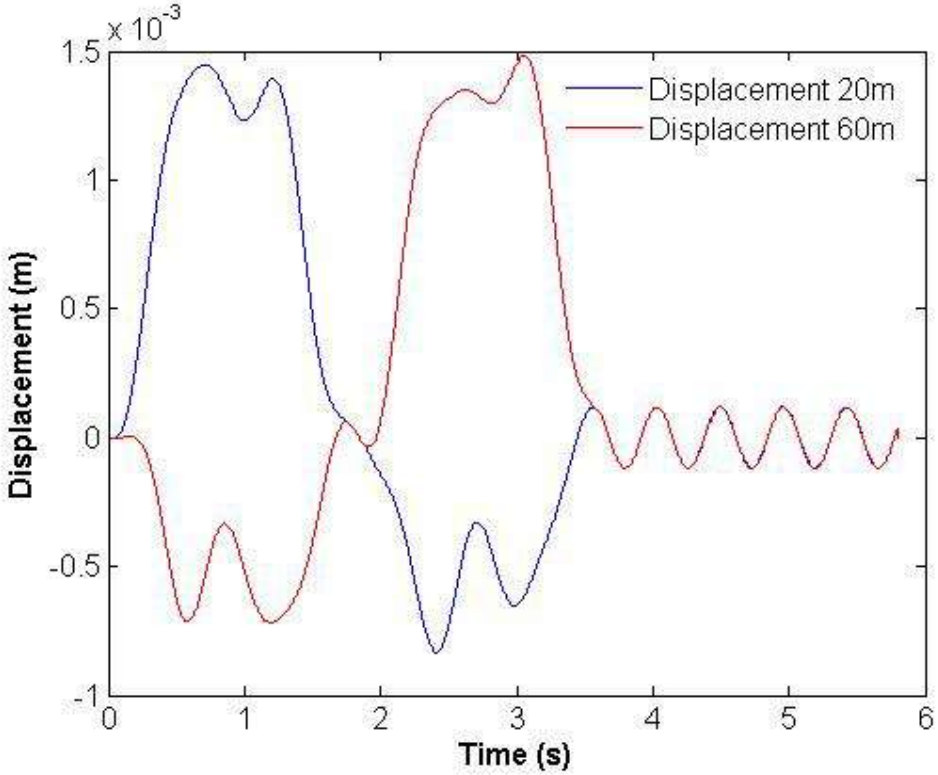

Figure 6.5 – Displacement at 20 m (blue) and 60 m (red) due to a constant load of 100000 N travelling at 22 m/s

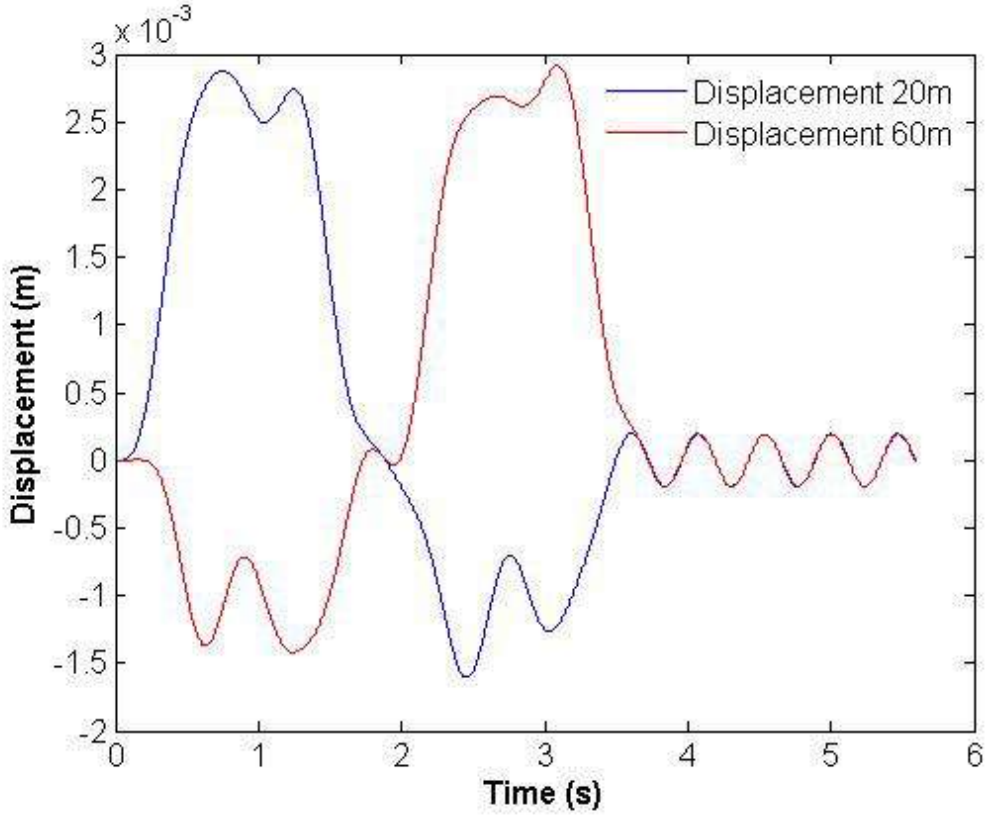

Figure 6.6 – Displacement at 20 m (blue) and 60 m (red) due to a constant load of 100000 N travelling at 22 m/s

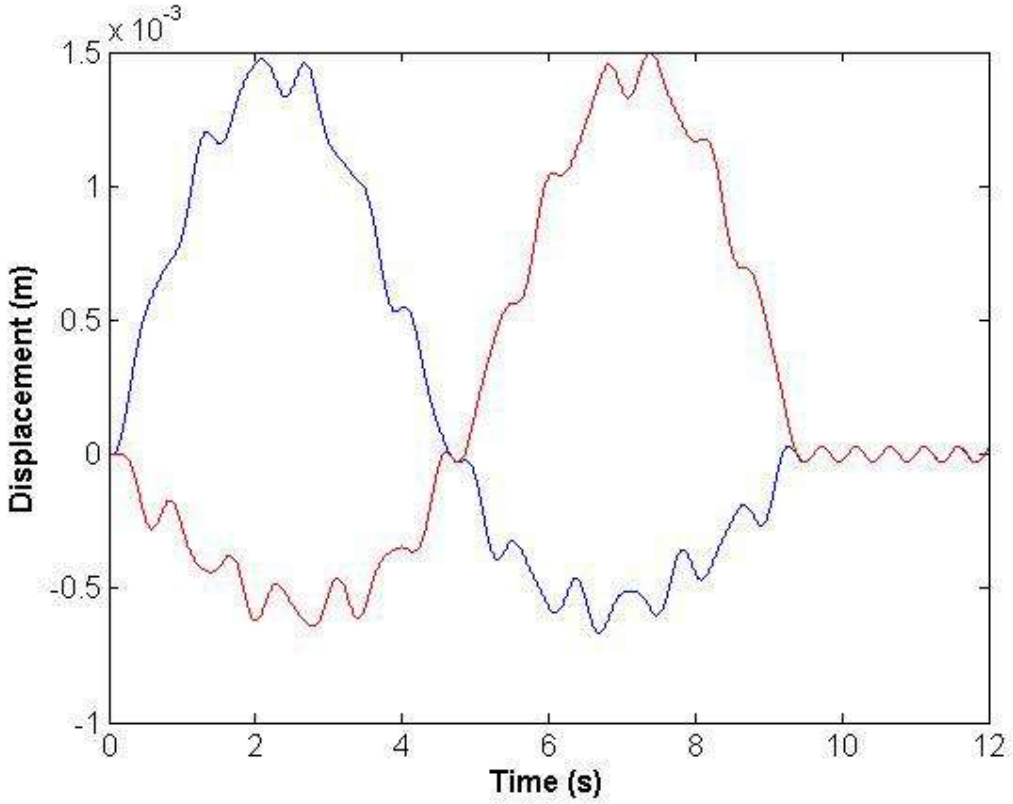

Figure 6.7 – Displacement at 20 m (blue) and 60 m (red) due to a constant load of 100000 N travelling at 8.46 m/s

Simulations for the remaining two velocities were analysed for a single moving load of 100000 N, using the decoupled equations of motion and the modal contributions of the first three modes (z_1, z_2, z_3) were plotted against time. From this analysis it was found that, at the instant when the force exits the bridge deck, the modal contributions of modes one and three are zero, and the free vibration is solely due to the second natural frequency, see figures 6.8 and 6.9.

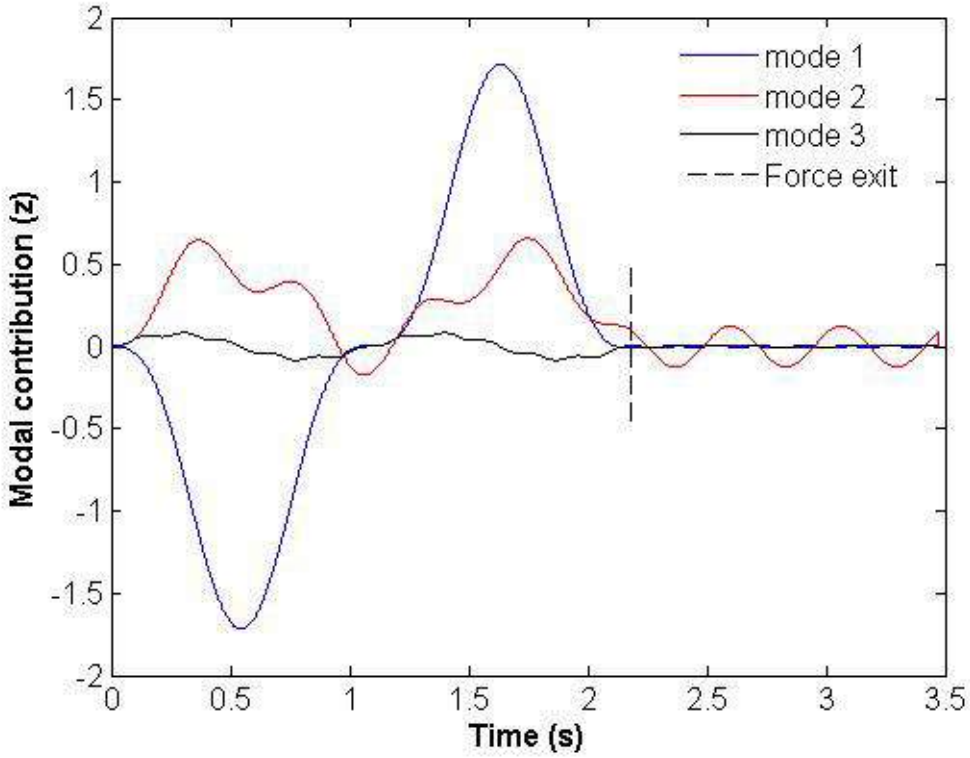

Figure 6.8 – First three modal coordinates versus time for a constant load of 100000N travelling at 36.7 m/s

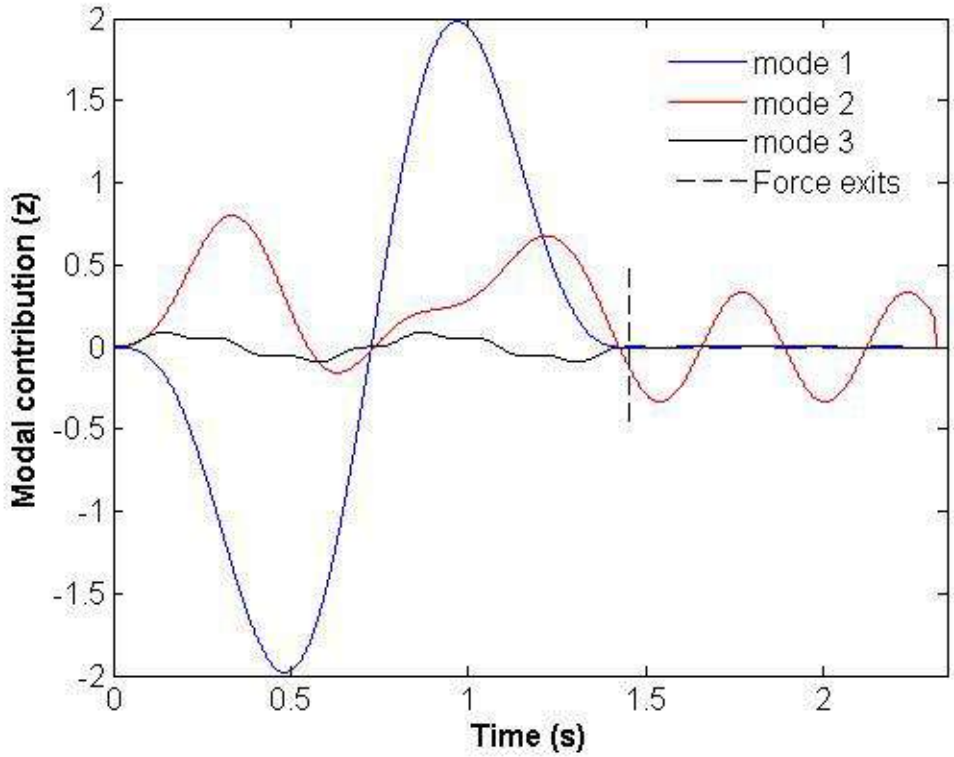

Figure 6.9 – First three modal coordinates versus time for a constant load of 100000N travelling at 55 m/s

6.4 Multiple Force Identification using an Eigenvalue Reduction Technique

The accuracy of the algorithm is tested using the method of simulation described in section (4.1). Two moving forces at a constant axle spacing of five metres are simulated traversing the beam. All simulations are carried out using the full stiffness and mass matrices. Three pairs of dynamic forcing functions are chosen to simulate the dynamics of a truck and to test the robustness of the algorithm. The three combinations are defined as:

$$\text{(i)} \qquad \begin{aligned} F_1(t) &= 70,000 + 14,000\sin(5\pi t) \\ F_2(t) &= 100,000 + 20,000\sin(5\pi t - \pi/2) \\ velocity &= 22m/s \end{aligned} \qquad (6.27)$$

$$\text{(ii)} \qquad \begin{aligned} F_1(t) &= 70,000 + 14,000\sin(5\pi t) + 5000\sin(30\pi t) \\ F_2(t) &= 100,000 + 20,000\sin(5\pi t - \pi/2) + 5000\sin(30\pi t) \\ velocity &= 20m/s \end{aligned} \qquad (6.28)$$

$$\text{(iii)} \qquad \begin{aligned} F_1(t) &= 60,000 + 12,000\sin(10\pi t) + 7200\sin(50\pi t) \\ F_2(t) &= 80,000 + 16,000\sin(10\pi t) + 12000\sin(50\pi t) \\ velocity &= 25m/s \end{aligned} \qquad (6.29)$$

The first combination is used to check if the MFI theory can identify moving forces with a dynamic component out of phase. The magnitude and frequency of the load is though to be representative of vehicle dynamics, it should also be noted that the velocity is 22m/s. The second load combination is to analyse for the effect of multiple truck frequencies, where the first frequency is out of phase and the second frequency is in phase. The final combination is for multiple frequencies both in phase, where both the magnitude and frequency of the dynamics is higher than the previous combinations. The simulated strains at 20.25 m, 30.25 m, 50.25 m and 60.25 m, contaminated with 3% Gaussian noise as defined in equation 4.28, are used as the "measurements" (see figure 6.9) for load combinations (i) and (ii).

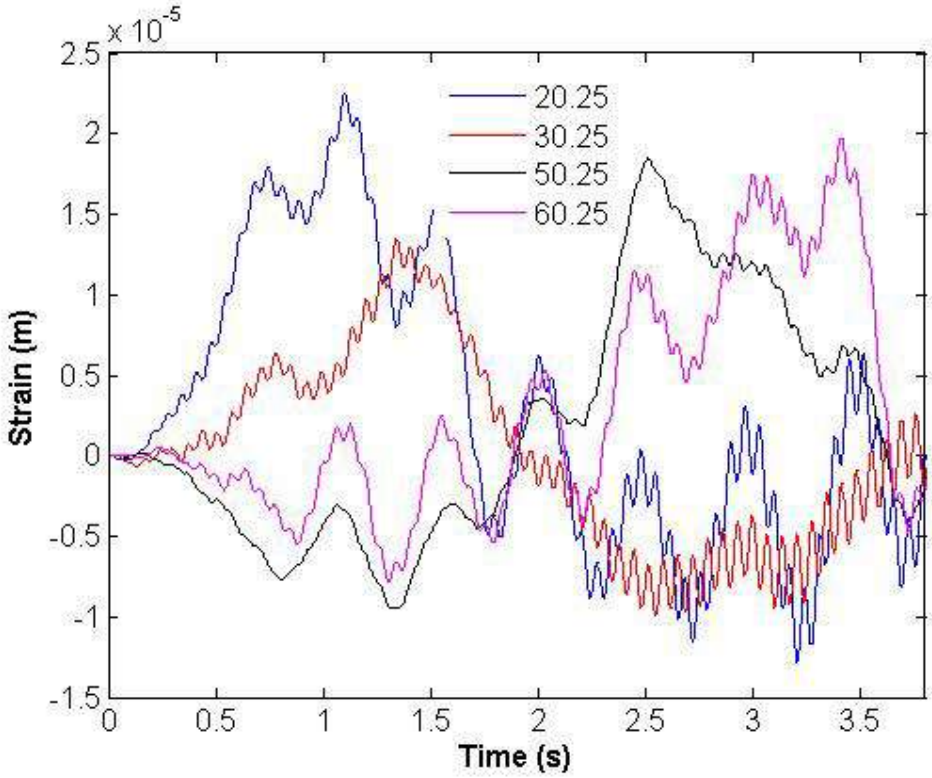

(a) – Theoretical Strain

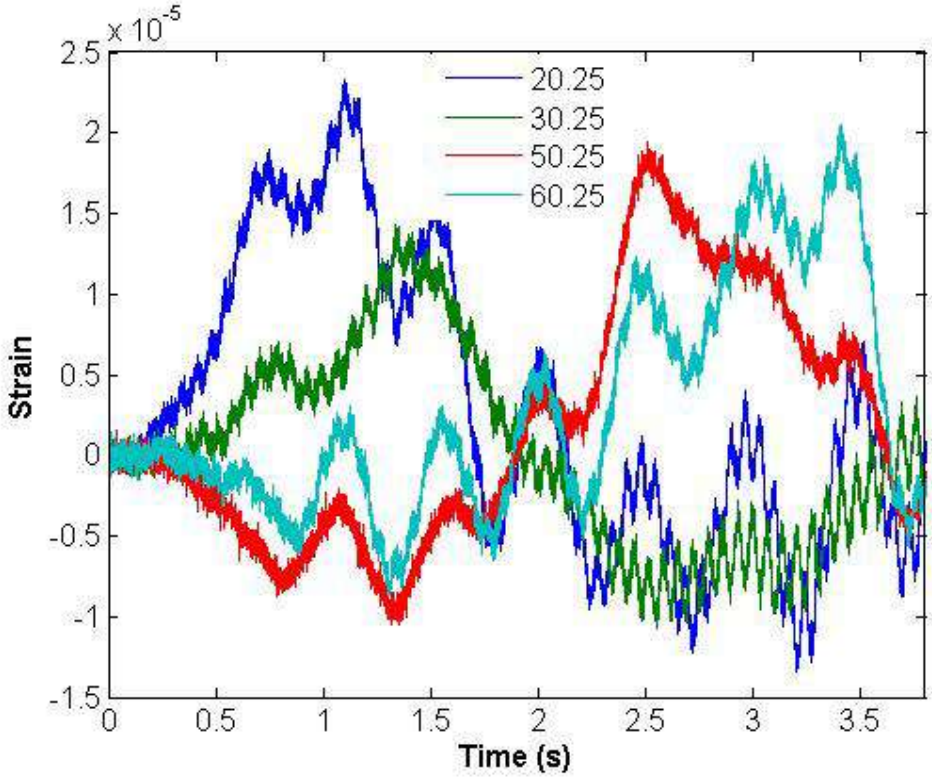

(a) – Noisy Strain

Figure 6.10 – Simulated Strain at 20.25 m, 30.25 m, 50.25 m and 60.25 m due to load combination (ii) travelling at 20 m/s

6.4.1 Inverse Model and Results

The bridge model described in section 6.3 has three boundary conditions for the supports at zero, forty and eighty metres. The numerical implementation of the boundary conditions for this bridge model would result in a discontinuity of the regularised forces. This is due to the fact that the dynamic programming routine would optimise for a force of zero as the axles traverse the support. The solution adopted for this problem is to replace the middle support with a very stiff spring, see figure 6.11. The entry in the stiffness matrix corresponding to the location of the middle support, was made large enough to be effectively infinitely stiff, but not so large as to cause numerical instability. The stiffness was also chosen such that the difference in dynamic simulations using both models minimised, a stiffness of 10^{17} kN/m was found to work well. A modal analysis is then performed on the finite element model and a discrete number of modes are used in the inverse solution. In this study, 25 modes of vibration are used for all inverse analyses.

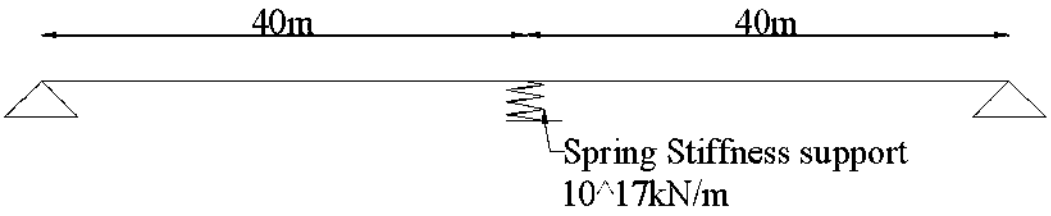

Figure 6.11 – Inverse model used for the two-span continuous bridge

The contaminated strains at 20.25 m, 30.25 m, 50.25 m and 60.25 m are used as the measurements for combinations (i) and (ii). The L-curve method is used to calculate the optimal regularisation parameter, and in some case's Hansens (1991) program 'plot_lc' has been used as a post processing tool to plot the norms calculated form the first order regularisations. The procedure for the first order regularisation is exactly the same as that outlined in Chapter 4. The optimal regularisation parameter for combination (i) found using the L-curve method as 1×10^{-17} using 25 modes of vibration, see figure

6.12. Using the optimal regularisation parameter combined with the dynamic programming routine and the first 25 modes of vibration, the optimal forcing functions are predicted. Figure 6.13 shows the predicted versus the theoretical forces for combination (i). Figure 6.13 shows that the MFI theory using the eigenvalue reduction technique performs reasonably well, particularly in the case of the second moving force, however the results for the first moving force are not as accurate, particularly at the start and end of the force time histories. These inaccuracies could be due to the velocity of 22 m/s or simply that 25 modes of vibration do not accurately represent the overall behaviour of the structure. The optimal regularisation parameter for combination (ii) is calculated approximate from the L-curve to be 1×10^{-18} respectively. Figures 6.15 (a) and (b) show the predicted versus the theoretical forcing function for combination (ii). The predicted force time histories for loading combination (ii) compare very well with the theoretically applied loads, aside from the period when the second axle enters the bridge, there is very good agreement between the theoretical and predicted forces. The MFI algorithm using an eigenvalue reduction technique can accurately identify the higher frequency of 15Hz and its magnitude.

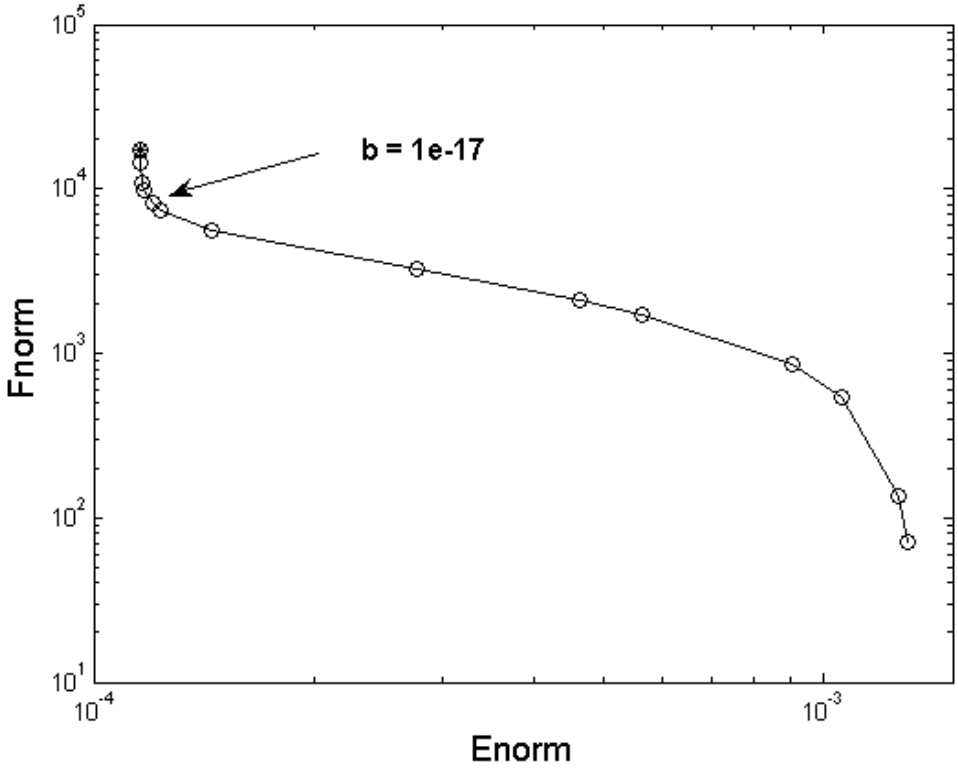

Figure 6.12 – L-curve for force combination (i)

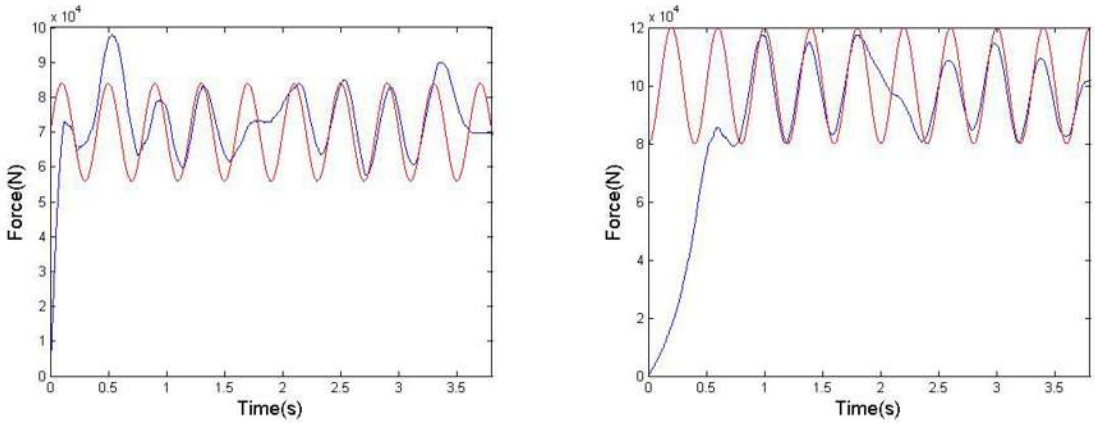

(a) (b)

Figure 6.13 – Regularised solutions for (a) front and (b) rear axle for force combination (i) (– theoretical force, – predicted force)

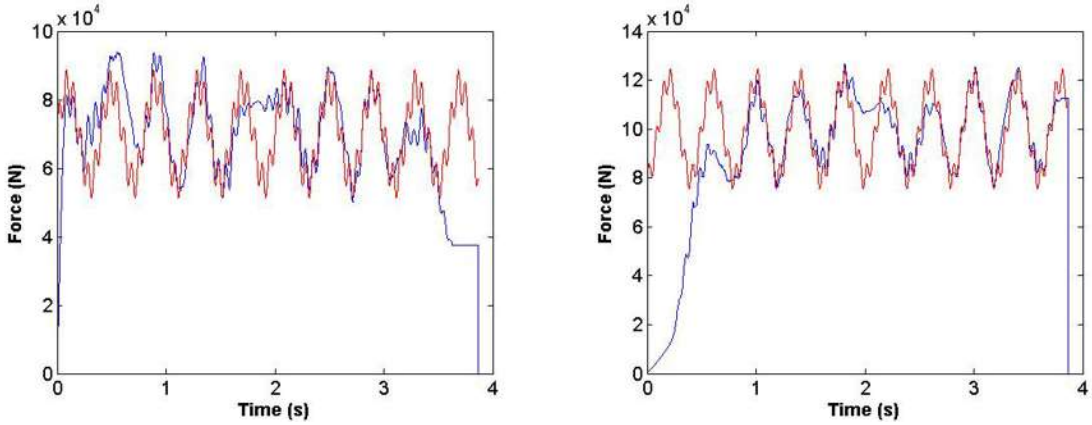

(a) (b)

Figure 6.14 – Regularised solutions for (a) front and (b) rear axle, for force combination (ii) (– theoretical force, – predicted force)

The displacements at 20 m, 30 m, 50 m and 60 m, contaminated with 3% gaussian noise are used as the measured inputs for combination (iii), see figure 6.15. It was observed using displacements as the measured input, that the results are more sensitive to the optimal regularisation parameter than that for strain. The optimal regularisation parameter using displacements was calculated approximately from the L-curve to be 2.7×10^{-15}, see figure 6.16. Figure 6.17 show the predicted versus the theoretical forcing function for combination (iii) using displacements as the "measurements". This figure illustrate that the use of displacements give excellent results, apart from the identified force histories at the start and end, the identified results are almost indistinguishable from the theoretical.

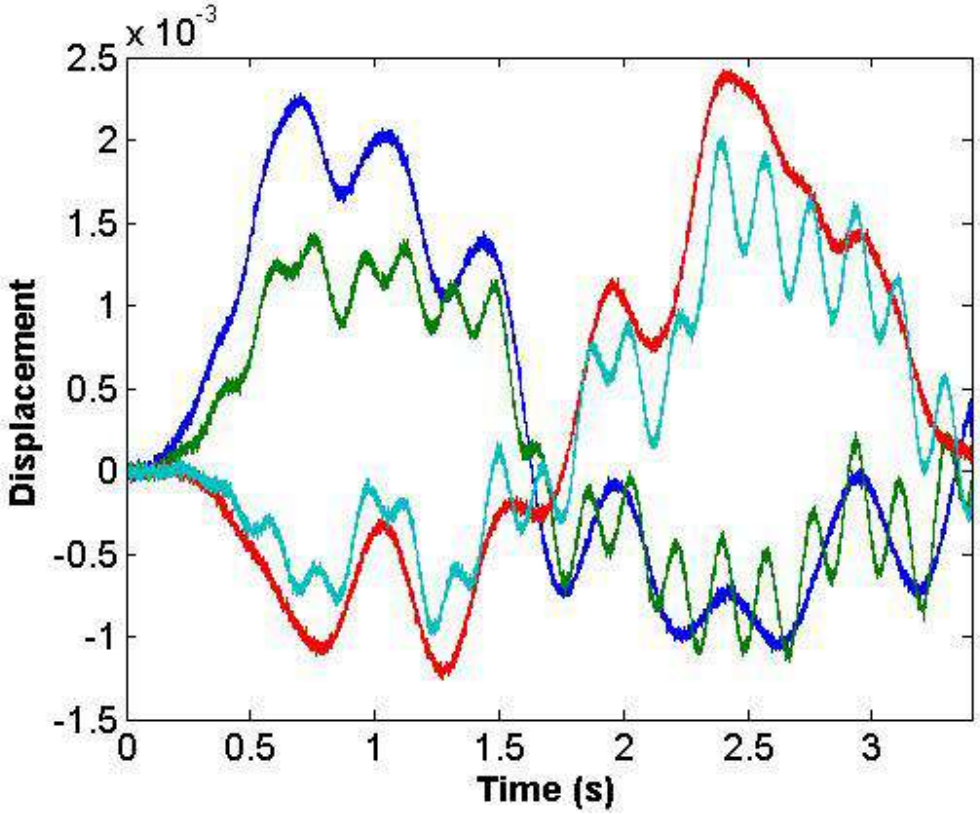

Figure 6.15 – Simulated noisy translations at 20 m, 30 m, 50 m and 60 m, due to load combination (ii)

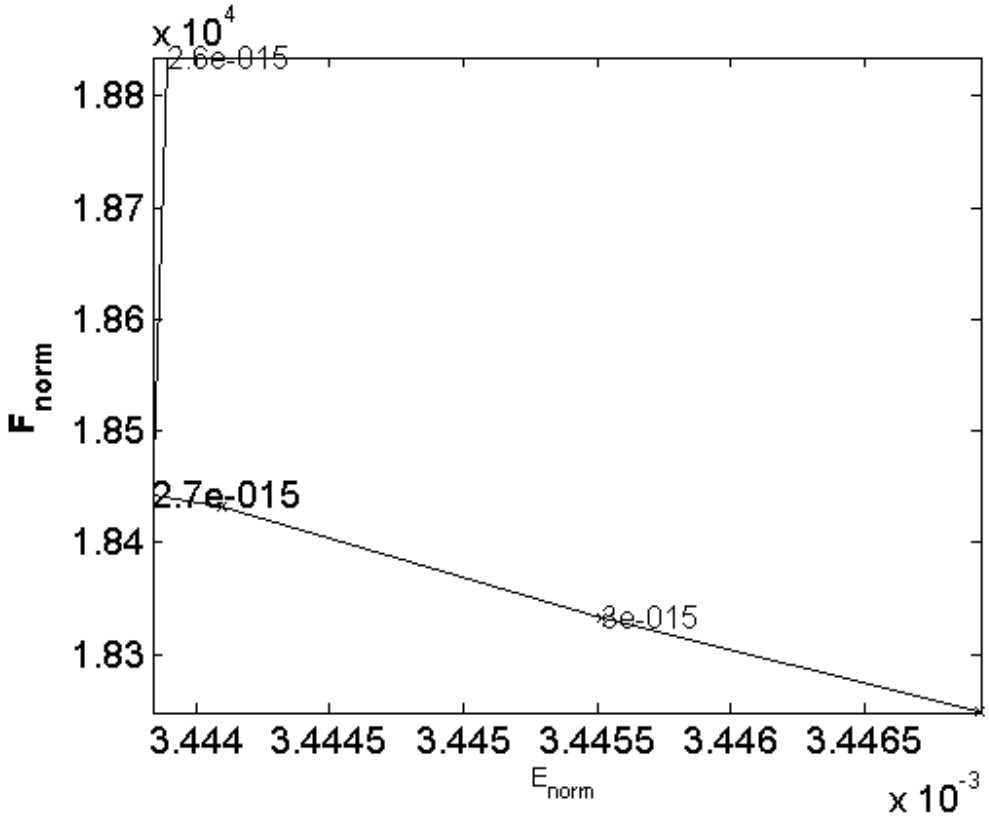

Figure 6.16 – L curve for force combination (iii) using translations as the 'measure' input

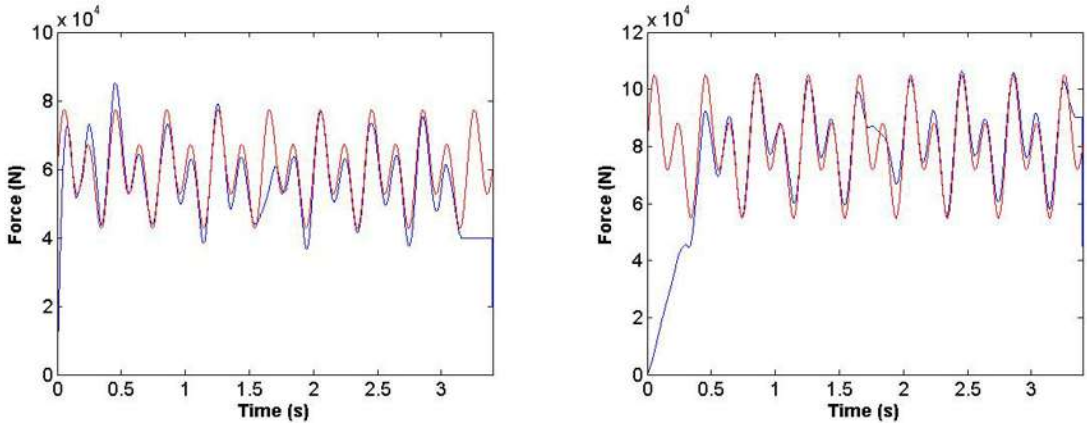

Figure 6.17 – Regularised solutions for (a) front and (b) rear axle for force combination (iii) (– theoretical force, – predicted force)

6.5 Study of the Eigenvalue Reduction

The robustness of the eigenvalue reduction technique is compared with the MFI algorithm outlined in chapter 4, which uses the full stiffness and mass matrices. The MFI algorithm using the eignevalue reduction technique, is further improved by removing the assumption made in chapter 4 that the elements of the FE model are sufficiently small such that whether or not the force *g(t)* is located at a node, it is assumed that it is sufficiently close to it that one can regularise as if the forces is actually at the node. It is now assumed that the force *g(t)* is distributed to the degrees of freedom of the particular element as a product of the shape functions. In this way the time-varying location matrix [*L(t)*] becomes a function of the Hermite shape functions of a 1d beam element defined by,

$$L(t) = \begin{bmatrix} 0 & 0 \\ . & . \\ N_1(x_1(t)) & . \\ N_2(x_1(t)) & . \\ N_3(x_1(t)) & N_1(x_2(t)) \\ N_4(x_1(t)) & N_2(x_2(t)) \\ . & N_3(x_2(t)) \\ . & N_4(x_2(t)) \\ 0 & 0 \end{bmatrix} \tag{6.30}$$

where column 1 represents the distribution of the first force to the degrees of freedom of the particular element that the force is acting on, $x_1(t)$ is the distance of the force from the left hand side of the element and N_1 to N_4 are the shape functions as defined in Appendix (C). Equivalently column 2 is for the second force of the vehicle.

The improved algorithm is first compared with the method of chapter four using the Fryba vehicle bridge interaction model and then with the bridge model outlined in sections 5.5 and 4.2. Analysis is carried out for two different scenarios of the vehicle bridge interaction model. The first represents an empty vehicle (2000 kg) moving at 15 m/s on a good profile, the theoretical strain measurements are generated using the program of (Gonzlaez 2001) and then contaminated with 3% Gaussian noise. The optimal regularisation parameter for the original algorithm was found to be 1×10^{-18}, and 1×10^{-18} for the eignevalue reduction technique. It should also be noted that the physical criterion used to obtain the optimal regularisation parameter in section 5.5 is no longer required and the L-curve alone is sufficient to obtain the optimal regularisation parameter, see figure 6.17. Figure 6.22 shows the theoretical and predicted forces for the original algorithm and the modified eigenvalue reduction technique.

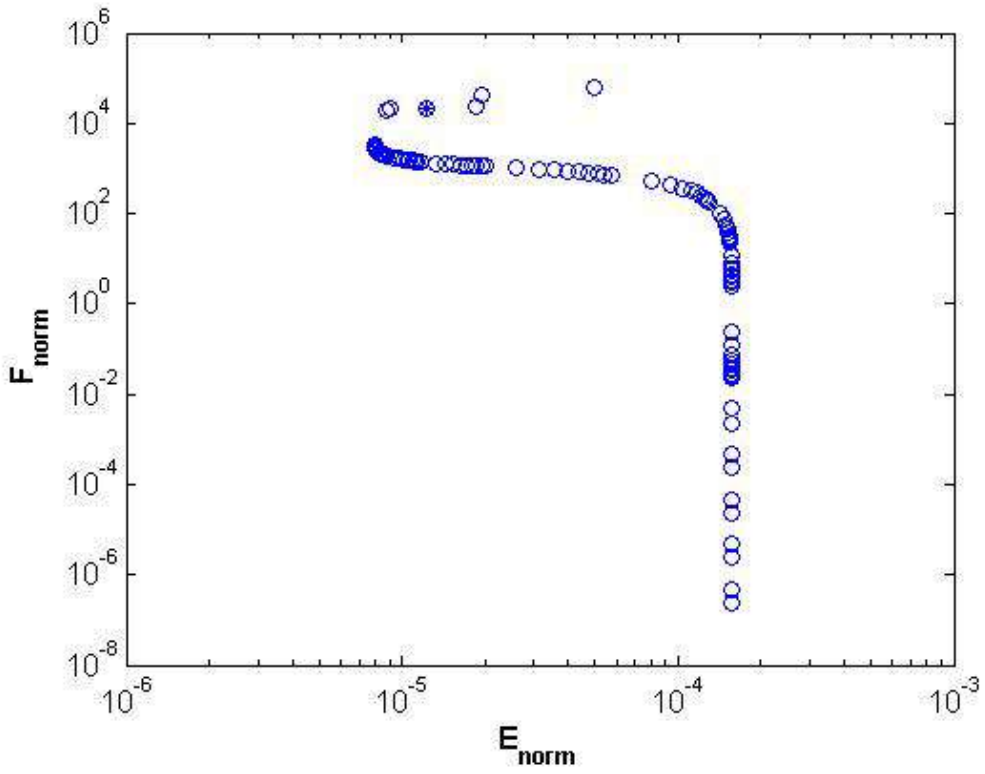

Figure 6.18 – L curve for an empty vehicle moving at 15 m/s on a smooth profile using the modified eigenvalue reduction technique

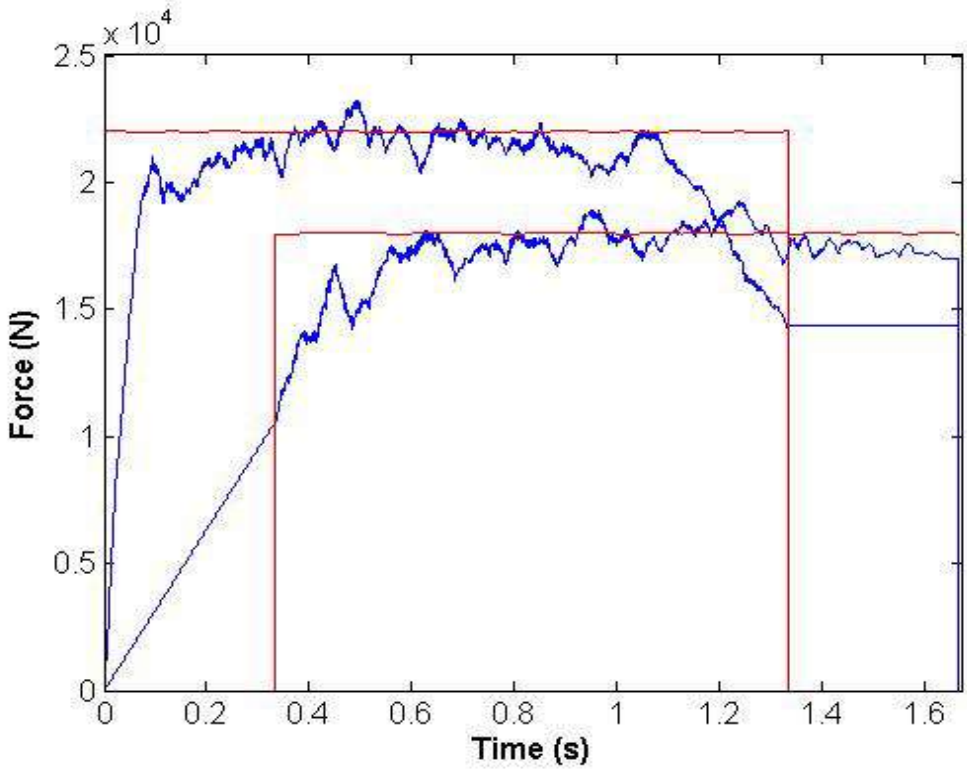

(a) – MFI algorithm of Chapter 5

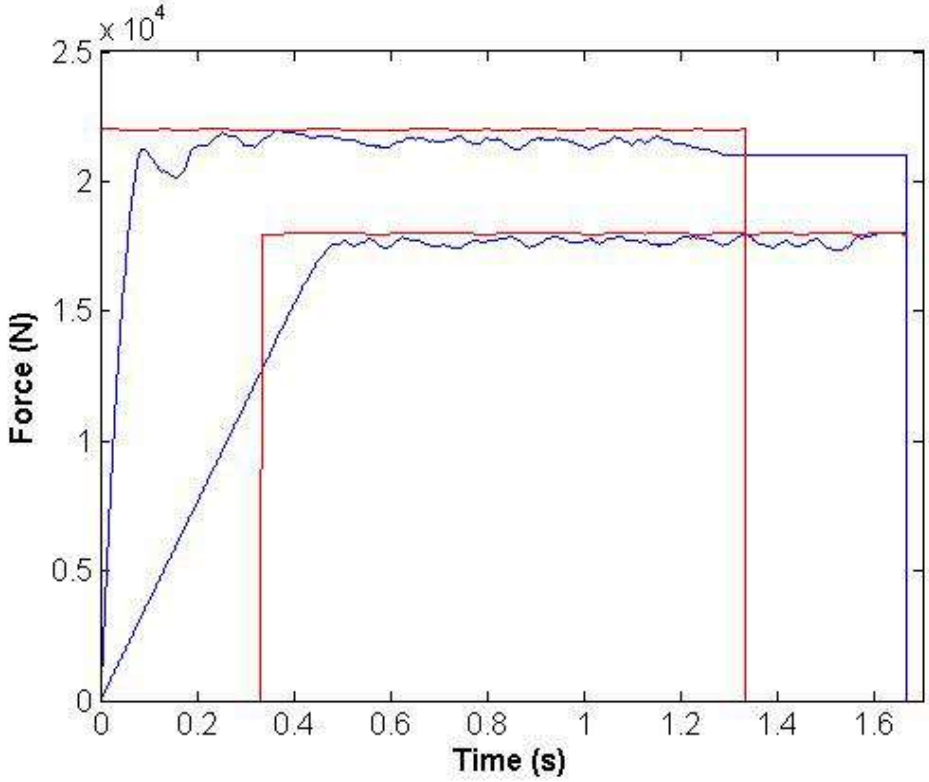

(b) - MFI using an eigenvalue reduction technique

Figure 6.19 – Predicted forces and applied forces for an empty vehicle moving at 20m/s on a good, $\lambda = 1 \times 10^{-18}$, (– theoretical force, – predicted force)

Figure 6.19 illustrates the effectiveness of the eigenvalue reduction technique coupled with the correct distribution of the forces to be predicted over that of the theory outlined in chapter 5. Although the identified results are smoother and the result is clearly more accurate over that of the algorithm of chapter 5 in both cases the MFI theory tends to slightly underestimate the applied forces.

The second example represents a fully laden vehicle of which the sprung mass is 14000 kg, the road roughness is poor as defined by the ISO and the vehicle is travelling at 25 m/s. The theoretical strain measurements are generated using the program of Gonzalez (2001) and then contaminated with 3% Gaussian noise. The optimal regularisation parameter for the original algorithm was found to be 1.7×10^{-19} using the criterion outlined in chapter 5, and approximately and 1×10^{-19} for the eignevalue reduction technique using the L-curve alone. Figures 6.20 to 6.21 show the theoretical and predicted forces for the original algorithm and the modified eigenvalue reduction technique.

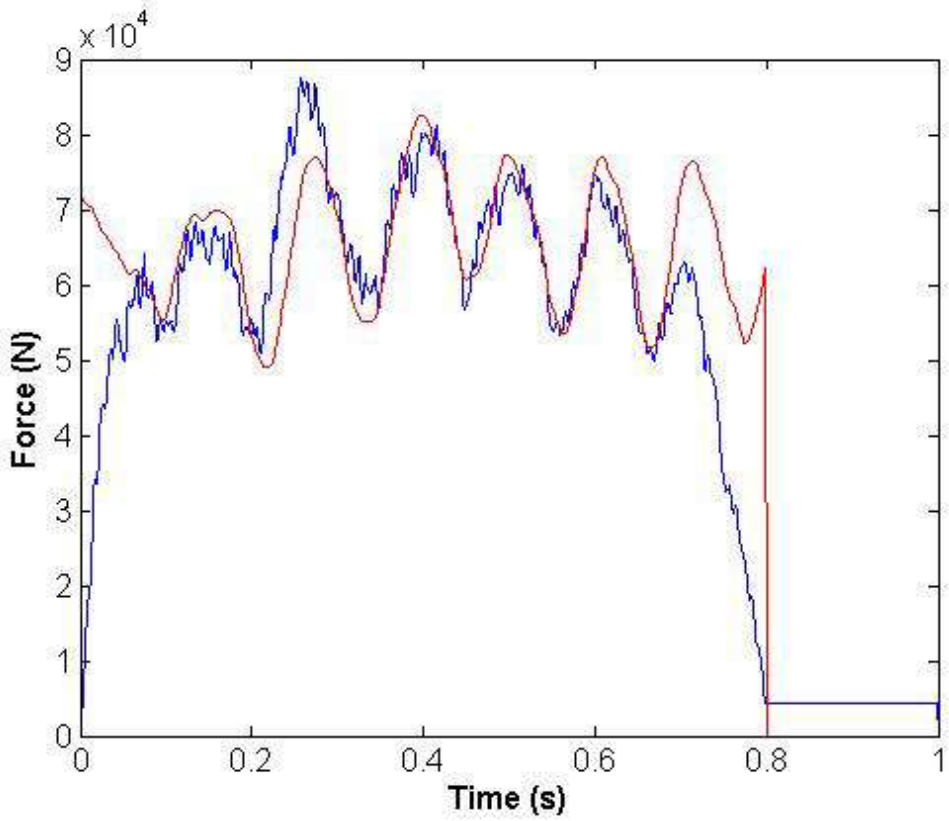

(a) –MFI using theory of Chapter 5, $\lambda = 1 \times 10^{-19}$, (– theoretical force, – predicted force)

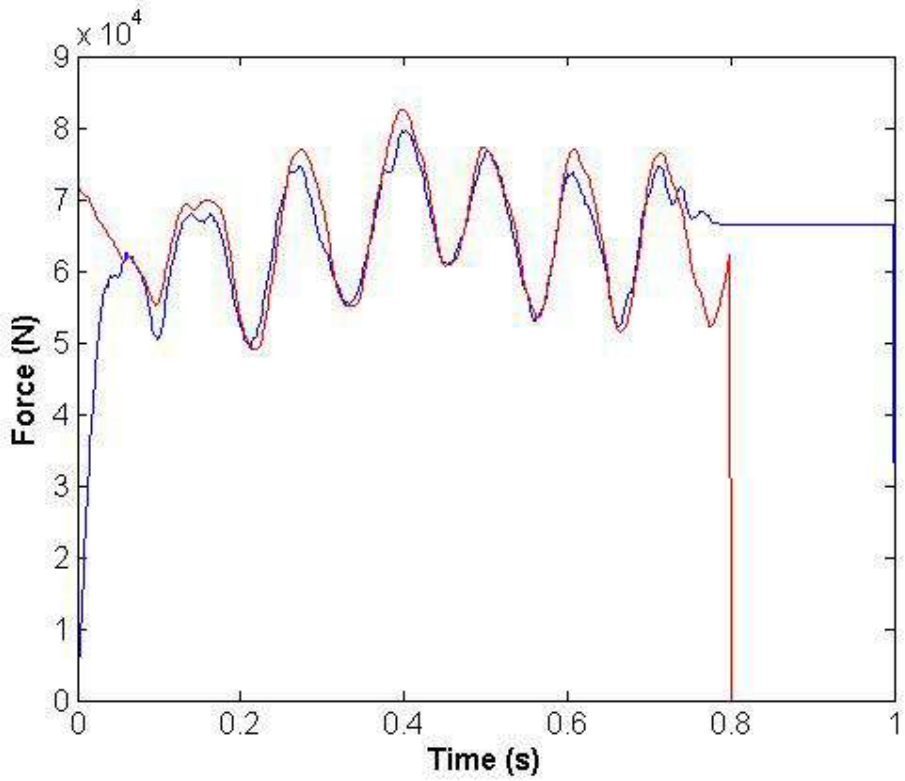

(b) –MFI using modified eigenvalue reduction technique, $\lambda = 1 \times 10^{-19}$, (– theoretical force, – predicted force)

Figure 6.20 – Regularised solutions for the front axle of a fully laden vehicle travelling at 25m/s on a poor road profile

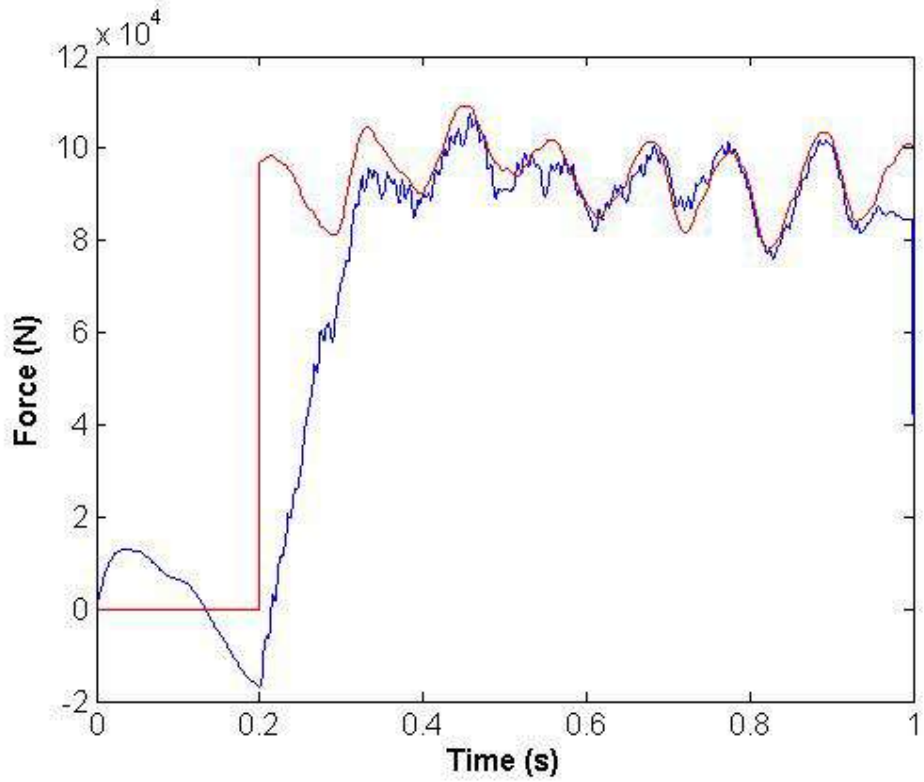

(a) - MFI using theory of Chapter 5, $\lambda = 1 \times 10^{-19}$, (– theoretical force, – predicted force)

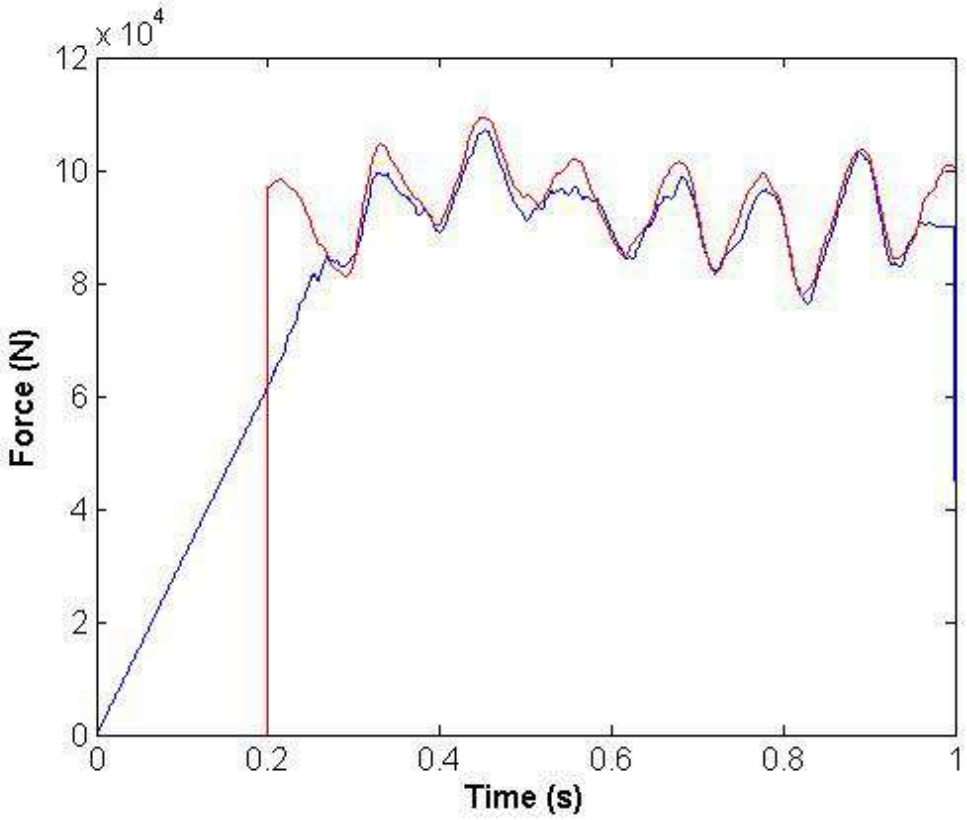

(b) –MFI using modified eigenvalue reduction technique, $\lambda = 1 \times 10^{-19}$, (– theoretical force, – predicted force)

Figure 6.21 – Regularised solutions for the back axle of a fully laden vehicle travelling at 25m/s on a rough profile

Figures 6.21 and 6.22 again illustrate the effectiveness of the modified eigenvalue reduction technique over that of the MFI theory of chapter 5. The results for the front and rear axle of the fully laden vehicle are distinctly smoother and more accurate over those of the theory in Chapter 5. In particular there is almost an exact match between the identified and applied forces in the front axle.

6.5.1 Error Analysis

The 20 m span, simply supported bridge model outlined in section 4.2 is considered again here but subject to two moving forces defined by,

$$\begin{aligned} F_1(t) &= 70,000(1+.1\sin(10\pi t)+.05\sin(40\pi t)) \\ F_2(t) &= 100,000(1-.1\sin(10\pi t)+.05\sin(50\pi t)) \end{aligned} \tag{6.31}$$

The forcing functions are chosen as they are similar to those used in previous studies on the moving force identification problem (Zhu & Law 2000, Law & Fang 2001). The strains at 5 locations on the bridge, 4, 8, 10, 12 and 16 m are simulated using the full stiffness and mass matrices and the method of simulation outlined in section 4.2. The inverse model is descretized into 40 equal beam elements and an eigenvalue analysis is then performed. A discrete number of modes and a combination of 'measurements' are then used in all inverse solutions. Noise is added to the simulated signals in all cases as defined in equation (4.28). The error in identified forces is defined as (Zhu & Law 2000, Zhu 2001),

$$Error = \frac{\| F_{true} - F_{identified} \|}{\| F_{identified} \|} \times 100 \tag{6.32}$$

where ||.|| denotes the Euclidean norm of the vector, and F_{true} and $F_{identified}$ are the true and identified forces respectively.

6.5.2 Effect of Modal Truncation

In all cases the 'measured' strain signal is simulated using the full global stiffness and mass matrices. However in the inverse analysis, a finite number of modes are used. It is therefore necessary to establish the minimum number of modes required for an acceptable solution to be obtained. The effect of modal truncation is analysed for the scenario of a vehicle travelling at 25 m/s with an axle spacing of 5 m subject to the forcing functions defined in equation (6.31). The sampling frequency is .0005 s and 3% Gaussian noise has been added to the simulated strain at the 5 locations. All 5 'measurement' points have been used in the inverse analysis. Figures 6.22 and 6.23 show the percentage error as defined in equation 6.31 versus the number of modes used in the inverse analysis. It can be seen from this figure that when a minimum of between 20 and 25 modes is used in the analysis the error in identified axle forces has also reached a minimum. The error in predicted forces using the full stiffness and mass matrices is 12.98% for axle 1 and 9.48% for axle 2. Figure 6.24 shows the predicted force versus the theoretical force using 25 modes of vibration in the inverse analysis with errors of 12.32% and 9.07% in the front and back axles respectively. The identified forces compare very well with the applied forces over the time period that both forces

are on the bridge. It can be seen that a significant proportion of the error is due to the initialisation of the dynamic programming routine at the start and end of the identified force time histories.

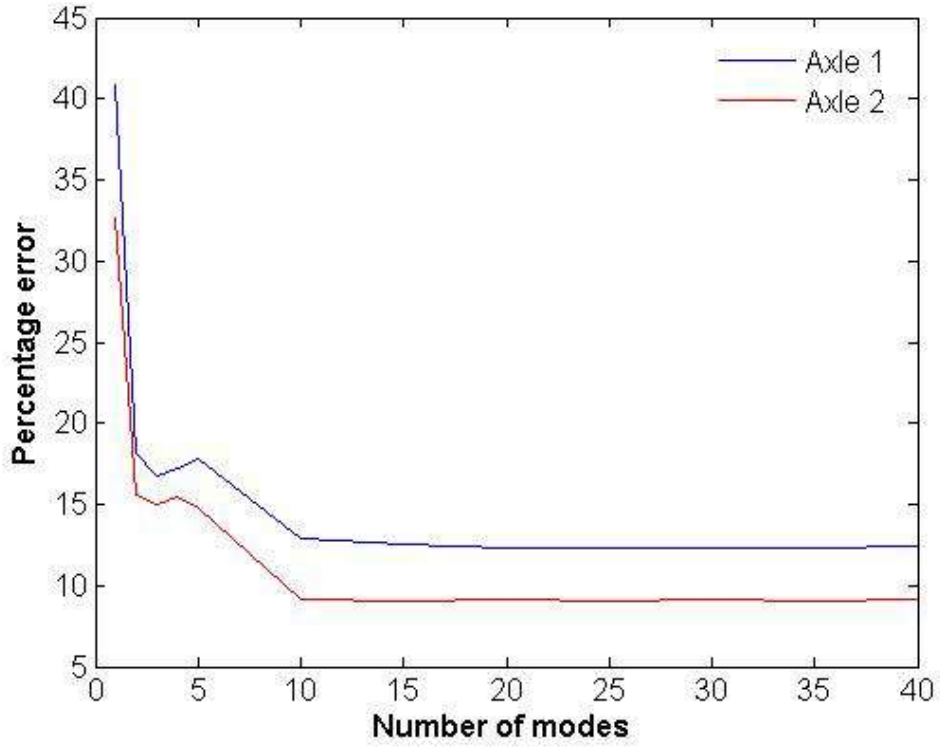

Figure 6.22 – The percentage error in predicted Forces versus the number of modes used in the inverse analysis

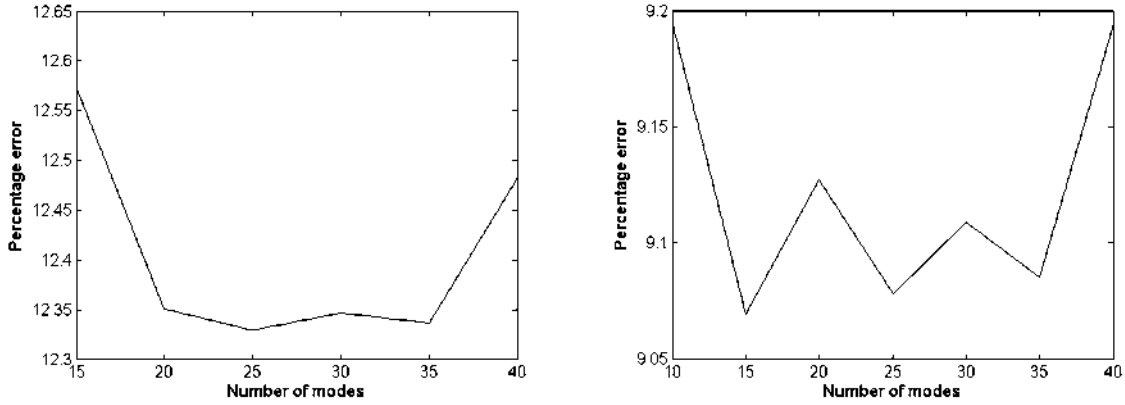

(a) - Axle 1 **(b)** – Axle 2

Figure 6.23 – The percentage error in predicted Forces versus the number of modes used in the inverse analysis

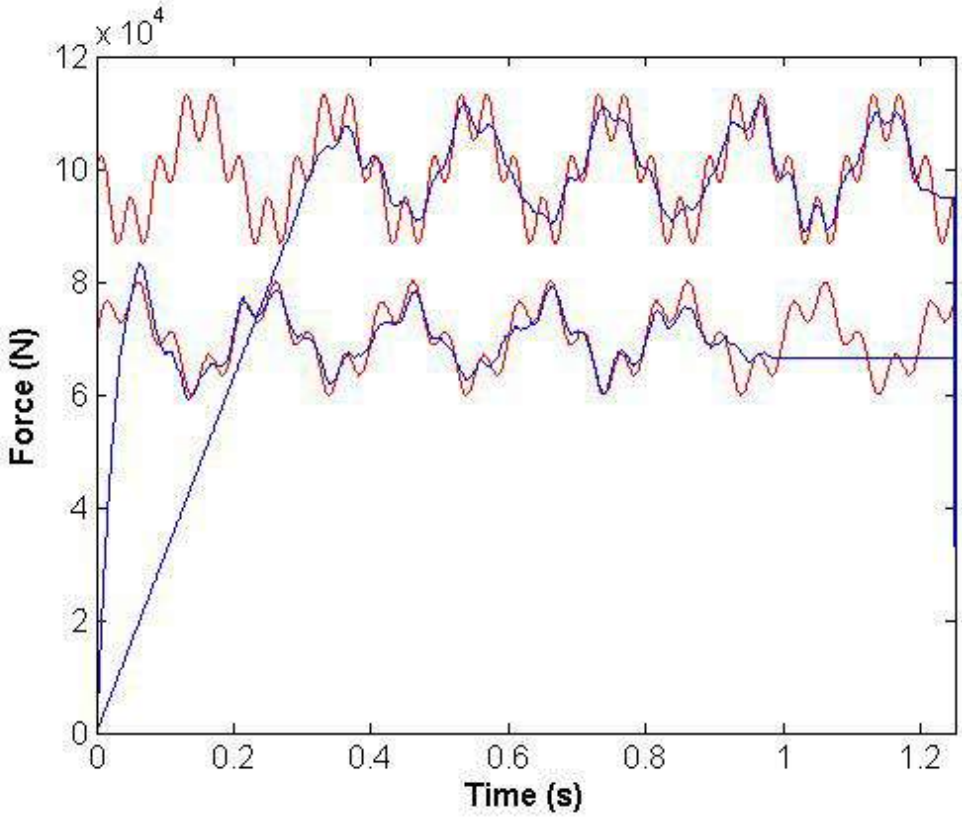

Figure 6.24 – Regularised solution using 25 modes of vibration in the inverse analysis.

The eigenvalue reduction technique results in a significant reduction in computational time with little or no loss in the predicted error provided about 20 or 25 modes are used in the inverse analysis. For example, using the full stiffness and mass matrices, takes approximately 6696 seconds whilst the program takes approximately 231 seconds when 20 modes of vibration are used, and 406 seconds when 25 modes are used in the analysis. In all of these cases 93 regularisation parameters have been used to calculate the optimal regularisation parameter. This is almost a 95% reduction in the computational time required with little loss in accuracy. Figure 6.25 shows the computational time taken for each L-curve analysis, where 93 regularisation parameters are used and the number of modes is varied from 1 to 40, the computational time taken for the L-curve using the full stiffness and mass matrices is also included.

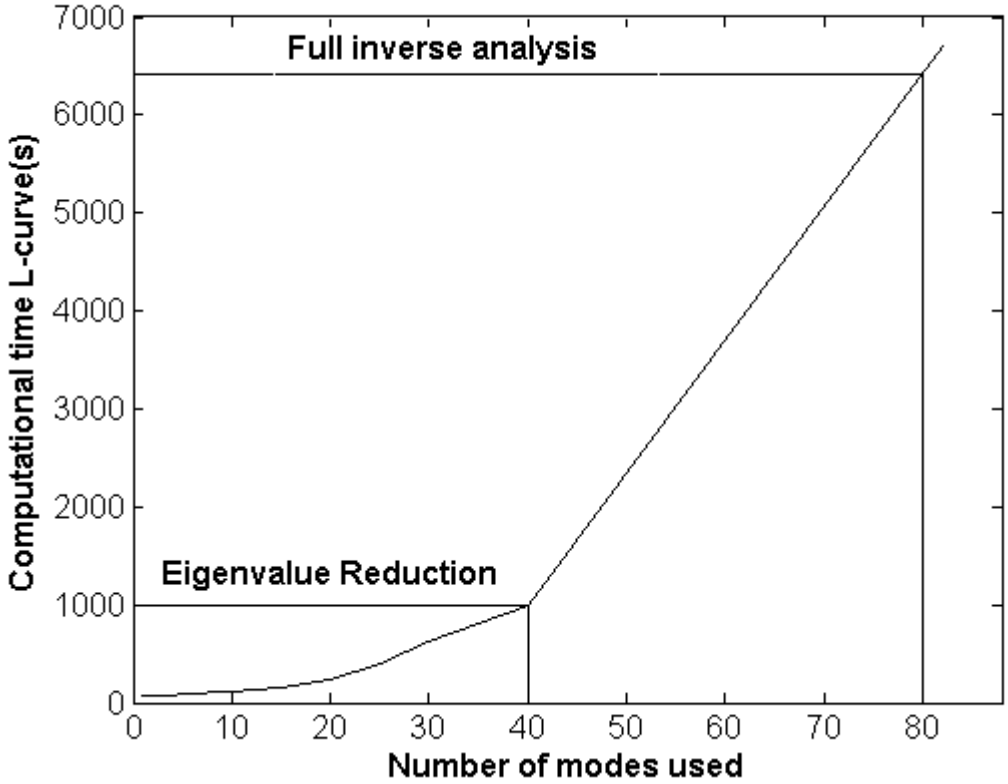

Figure 6.25 – Computational time for L-curve versus number of discrete modes used in the inverse analysis.

6.5.3 Optimal Location and Number of Sensors

The effect of the number and location of sensors used in the inverse analysis is investigated in this section. The effect of various sensor combinations is analysed for the scenario of a vehicle travelling at 25 m/s with an axle spacing of 5 m subject to the forcing functions defined in equation (5.31) on the bridge described in section 4.2. The sampling frequency is .0005 s and 3% Gaussian noise has been added to the simulated strain for the particular combination used in each inverse analysis. In all analyses 25 modes of vibration have been used. Various locations are analysed for 1,2,3,4 and 5 sensors used in the inverse analysis. Table 6.1 shows all of the sensor combinations tested for, and their equivalent errors for axle one and axle two.

Number of Sensors	Location	$\lambda \times 10^{-19}$	Axle 1 % Error	Axle2 % Error
1	4	4	36.2	22.1
	8	5	31.9	26.0
	10	7	30.5	29.9
	12	20	32.1	32.2
	16	5	28.7	33.5
2	4 and 8	9	15.1	10.9
	8 and 10	10	17.9	18.0
	10 and 12	10	16.0	18.7
	12 and 16	10	18.1	23.5
	4 and 10	10	16.3	10.8
	8 and 12	9	15.2	16.3
	10and 16	10	16.4	20.0
	4 and 16	2	12.2	8.9
	8 and 16	5	16.7	14.4
3	4,10 and 16	5	12.7	9.3
	8,10 and 12	60	17.9	18.8
	4,10 and 12	6	13.4	9.2
	8,10 and 16	7	14.3	17.2
	4,8 and 16	7	13.3	9.8
	4,8 and 10	9	16.5	10.3
	10,12 and 16	1	15.0	18.1
	4,12 and 16	7	13.0	9.5
	8,12 and 16	5	13.4	15.9
	4,8 and 12	4	13.2	8.8
4	4,8,10 and 12	5	12.9	8.8
	8,10,12 and 16	7	13.1	16.1
	4,10,12 and 16	7	12.5	9.2
	4,8,10 and 16	7	12.8	9.4
	4,8,12 and 16	7	12.8	9.4
5	4,8,10,12 and 16	9	12.3	9.0

Table 6.1-Errors in identified forces for various sensor combinations

It was found that for acceptable results to be obtained, the minimum number of sensors should be at least equal to the number of forces. In general it was found that the error in predicted forces decreases as the number of measurement locations increases, see table 6.1. However for various combinations tested there was an optimum combination of locations found corresponding to 2, 3 and 4 measurement locations. Therefore in the following error analysis there will be four sensor sets used for each inverse analysis see table 5.2, to ascertain which sensor set performs the best overall.

Optimal sensor Sets	Location
Sensor Set I	4,16
Sensor Set II	4,10,16
Sensor Set III	4,10,12,16
Sensor Set IV	4,8,10,12,16

Table 6.2 – Optimal combinations for the number of sensors used

Figure 6.26 shows the predicted force versus the theoretical force for sensor set I using 25 modes of vibration in the inverse analysis. The errors are 12.2% and 8.9% in the front and back axles respectively. The errors in the identified forces are representative of the results obtained in the other 3 optimum sensor sets.

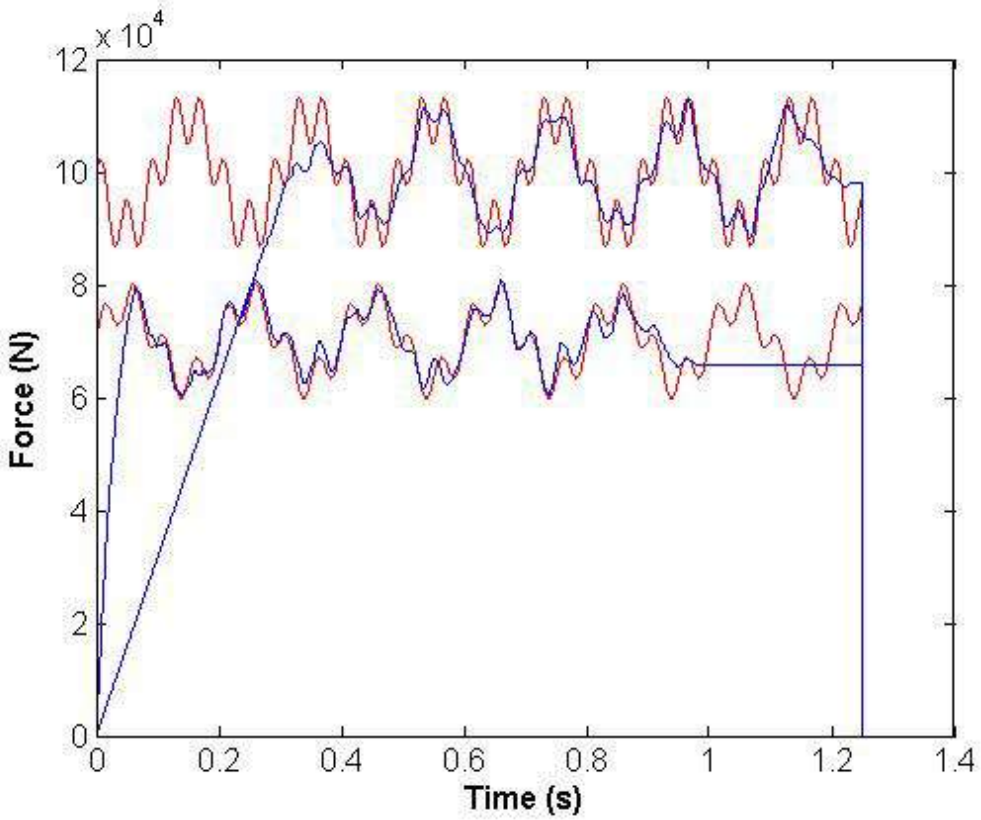

Figure 6.26 – Regularised solution using Sensor Set I

6.5.4 Effect of Velocity

The effect of vehicle velocity on the accuracy of the moving force identification algorithm is analysed for the scenario of a vehicle with constant axle spacing of 5m subject to the forcing functions defined in equation (6.31). Again the sampling frequency is .0005 s and 25 modes of vibration have been used in all inverse analysis. The velocity is varied from 10 m/s to 40 m/s in increments of 5; the four optimum sensor sets have been used in all of the inverse analysis, and each sensor set is contaminated with 3% Gaussian noise. Figure 6.27 shows the percentage errors in predicted forces for axles 1 and 2, versus the vehicle velocity for each of the optimum sensor locations. It can be seen from figure 6.27 that sensor sets III and IV perform poorly for vehicles travelling at velocities less than 15 m/s and sensor sets I and II in general give better results than III and IV. However for vehicle velocity greater or equal to 20 m/s, the percentage errors in identified results for all sensor sets are approximately equal.

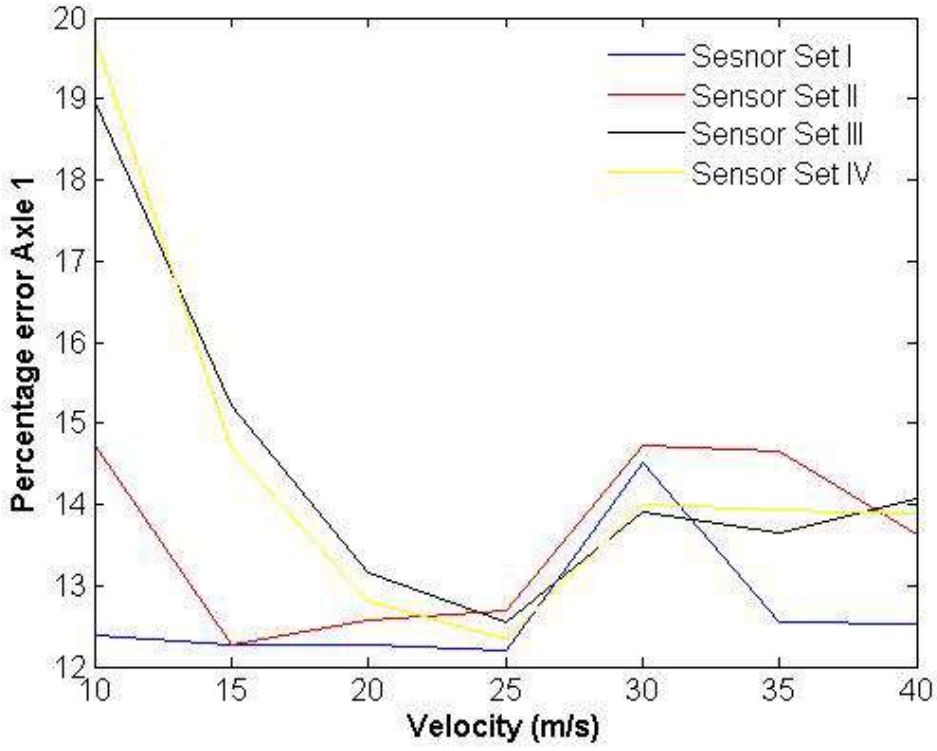

(a) – Axle 1

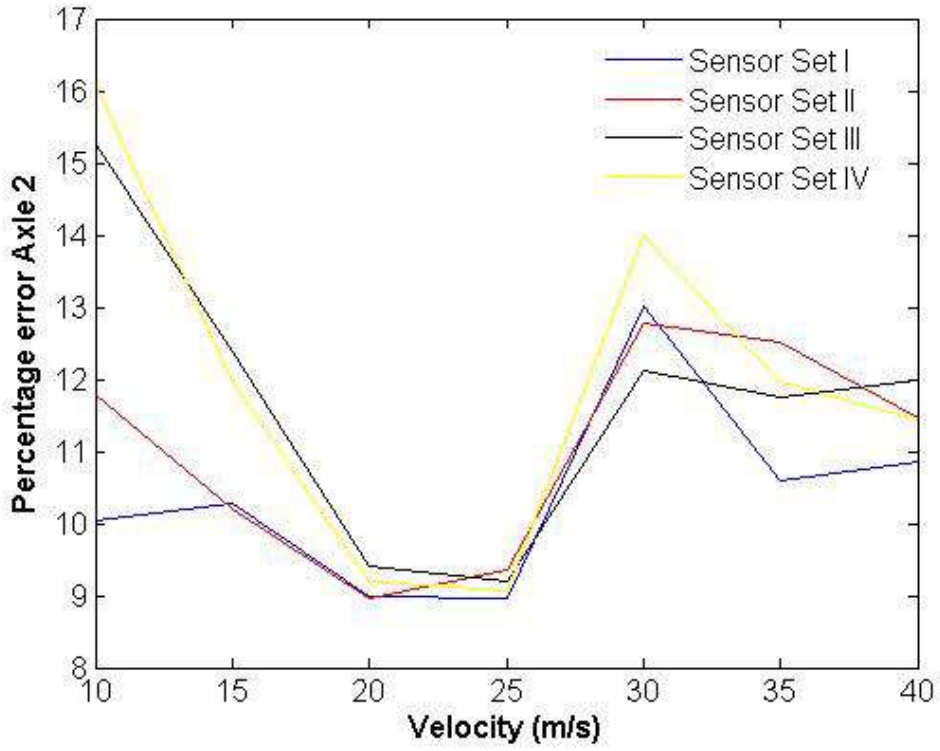

(b) – Axle 2

Figure 6.27 – Percentage error in identified forces versus vehicle velocity

It was also observed that for all sensor sets analysed, there is an increase in the error for the scenario of a vehicle travelling at 30 m/s. In general the errors in the predicted forces for a vehicle travelling at 30 m/s were found to be approximately 14% and 12% for axles one and two respectively. This could be attributed to the load circular frequency, which is 4.7Hz which in turn is quite close to the first natural frequency of the bridge of 4.3Hz.

6.5.5 Effect of Sampling Frequency

The effect of the sampling frequency on the accuracy of the moving force identification algorithm is analysed for the scenario of a vehicle moving at 20m/s with a constant axle spacing of 5m subject to the forces defined in equation (6.31). Again the four optimum sensor sets are used in each of the analysis carried out and 3% Gaussian noise is added to each sensor set combination. The sampling frequency is varied from 100 Hz to 500 Hz in increments of 100, and then from 500 Hz to 3000 Hz in increments of 500. As

previously 25 modes of vibration are used in all inverse analysis. Figure 6.28 shows the percentage errors in axles 1 and 2 versus the sampling frequency used in the inverse analysis. It can be seen from these figures that the accuracy of the moving force identification algorithm for this particular event is dependent upon the sampling frequency used, with the percentage errors in the MFI algorithm stabilising at approximately 1000Hz.

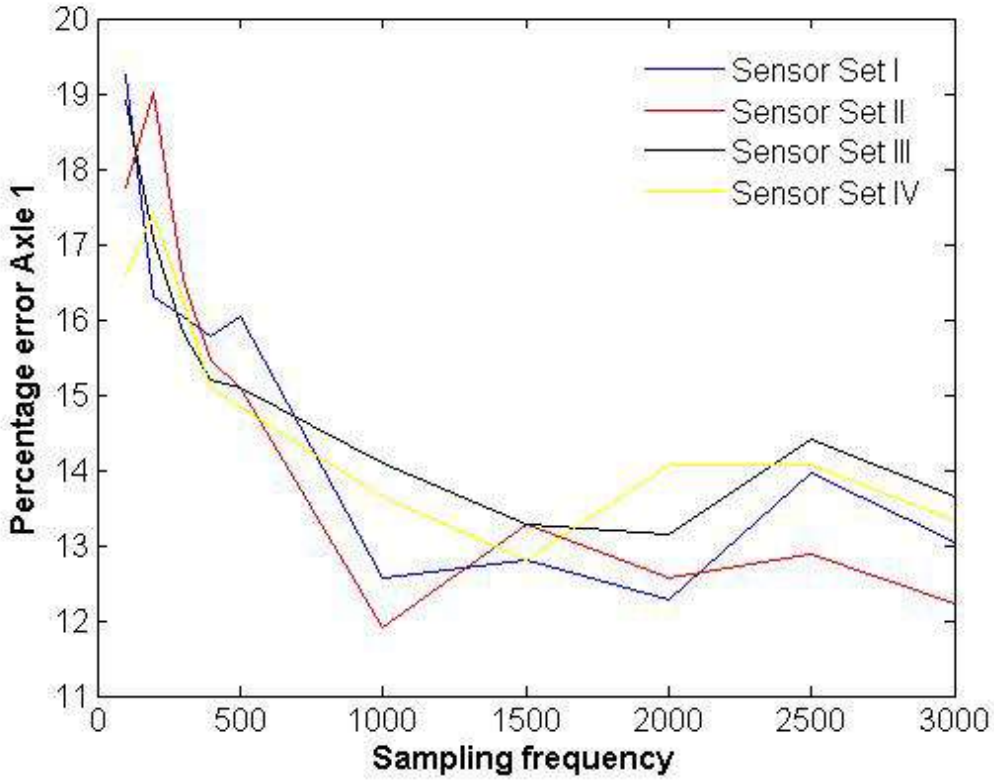

(b) – Axle 1

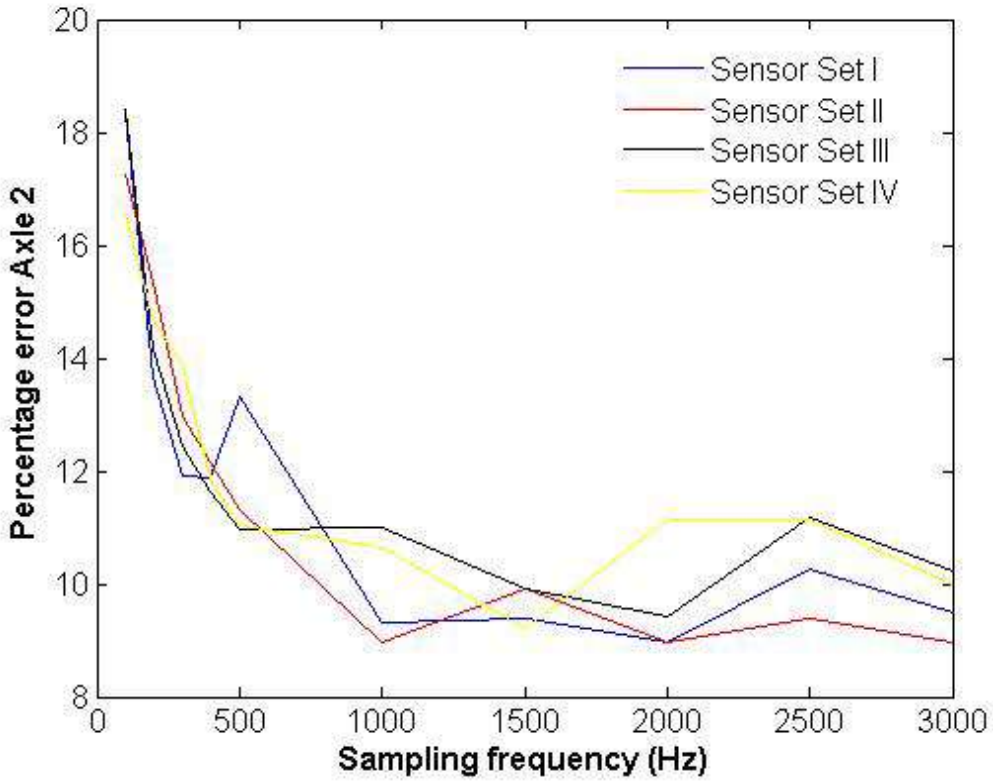

(b) – Axle 2

Figure 6.28 - Percentage error in identified forces versus the sampling frequency used in the inverse analysis

6.5.6 Effect of Noise

The effect of noise on the accuracy of the moving force identification algorithm is analysed for noise levels of 1% to 5 % in increments of 1, and the effect of 10% noise is also investigated, all for the scenario of a vehicle travelling at 20 m/s with an axle spacing of 5 m. The sampling frequency used in this inverse analysis is .0005 s, 25 modes of vibration have been used in all analyses, and for each level of noise levels the four optimum sensor locations have been used. Figure 6.29 and tables 6.3 to 6.6 show the percentage error in the predicted axle forces versus the percentage noise added to the simulated theoretical strain. In general the error in predicted forces increases in proportion to the percentage of noise added to the theoretical strain readings. It is thought that this increase in error is due to the fact that the greater the percentage noise added, the larger the least squared error norm, thus reducing the accuracy of the predicted solution. Figure 6.30 shows the L-curves for all noise levels of sensor set II. It is clear from these curves that, with each increase in the level of noise, the L-curve

shifts to the right thus reducing the norm of the error and increasing the error in the predicted forces. Also in general sensor sets I and II perform slightly better than sets II and IV, however it is thought that this is most likely due to the nature in which the noise is added. Sensor set I, uses 'measurement' locations at 4 m and 16 m along the 20 m simply supported beam, as noise is added as a percentage of the maximum strain induced in the particular sensor, the level of noise added to these sensors is significantly less than the level of noise added to the sensors located at 8, 10 and 12m and in particular the sensor at 10m.

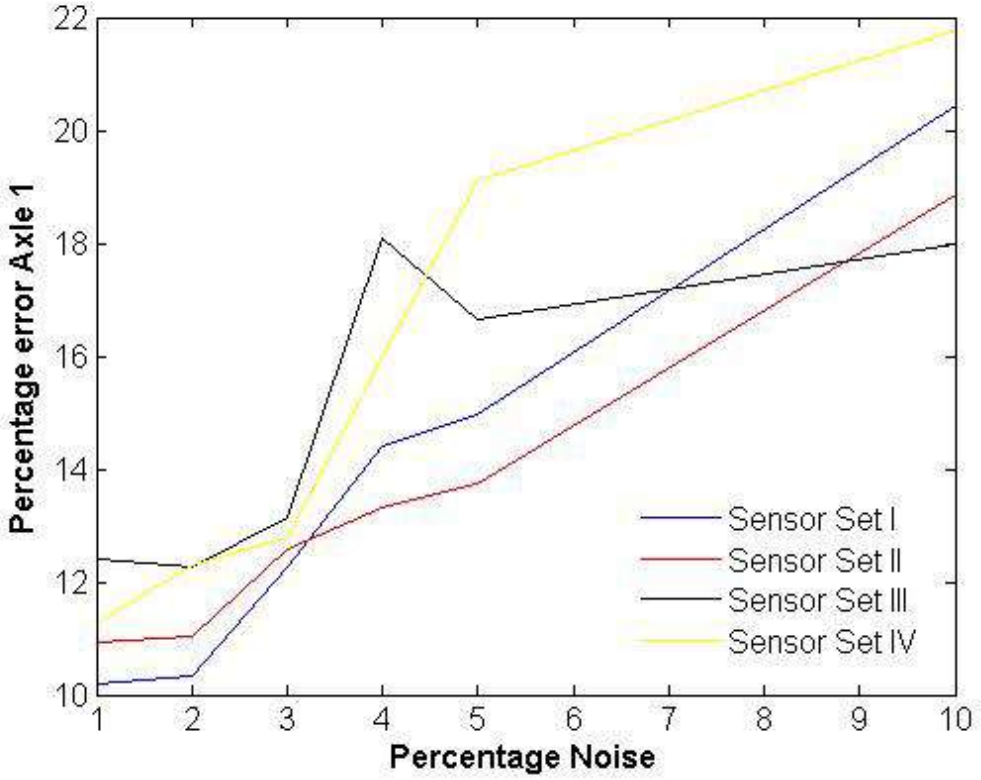

(a) – Axle 1

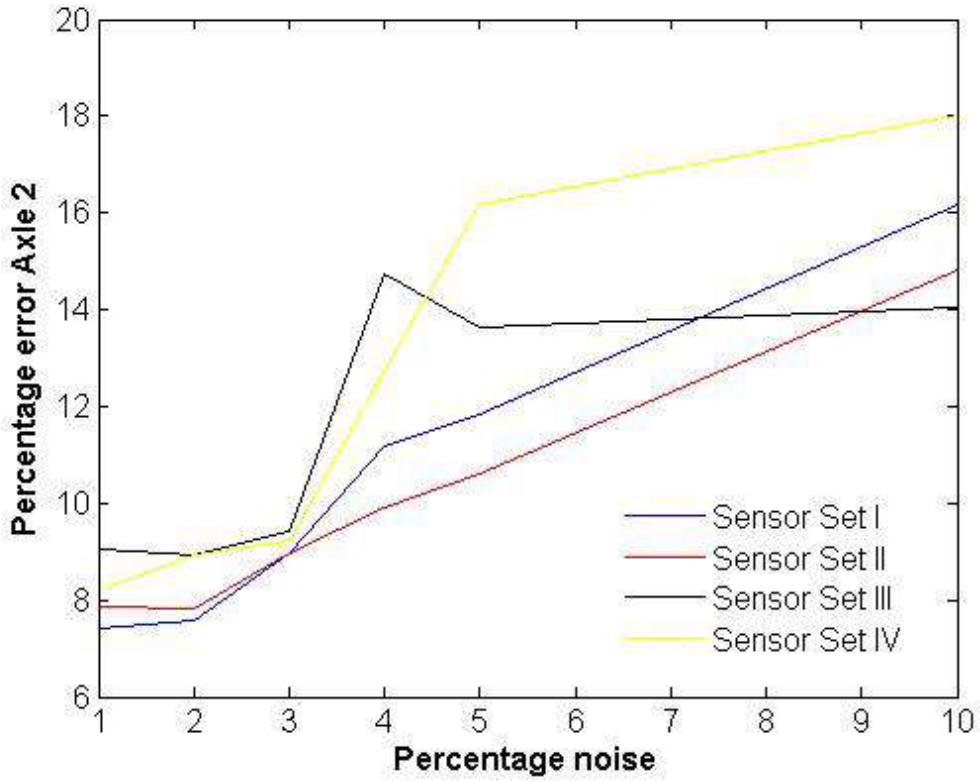

(b) – Axle 2

Figure 6.29 – Percentage error in the identified forces versus the percentage noise added to the optimum sensor sets.

Percentage Noise	λ	Axle 1 % error	Axle 2 % error
1	7×10^{-20}	10.1	7.3
2	1×10^{-19}	10.3	7.5
3	3×10^{-19}	12.2	8.9
4	8×10^{-19}	14.4	11.1
5	1×10^{-18}	14.9	11.8
10	8×10^{-18}	20.4	16.1

Table 6.3 - Percentage errors in the identified forces using Sensor Set I

Percentage Noise	λ	Axle 1 % error	Axle 2 % error
1	2×10^{-19}	10.9	7.8
2	2×10^{-19}	11.0	7.8
3	5×10^{-19}	12.5	8.9
4	9×10^{-19}	13.3	9.9
5	1×10^{-18}	13.7	10.6
10	8×10^{-18}	18.8	14.8

Table 6.4 - Percentage errors in the identified forces using Sensor Set II

Percentage Noise	λ	Axle 1 % error	Axle 2 % error
1	5×10^{-19}	11.4	8.3
2	7×10^{-19}	12.0	8.9
3	1×10^{-18}	13.1	9.4
4	9×10^{-18}	18.0	14.7
5	6×10^{-18}	16.6	13.6
10	8×10^{-18}	17.9	14.0

Table 6.5 - Percentage errors in the identified forces using Sensor Set III

Percentage Noise	λ	Axle 1 % error	Axle 2 % error
1	5×10^{-19}	11.2	8.1
2	8×10^{-19}	12.2	8.9
3	9×10^{-19}	12.7	9.2
4	5×10^{-18}	15.9	12.7
5	2×10^{-17}	19.1	16.1
10	4×10^{-17}	21.7	18.0

Table 6.6 - Percentage errors in the identified forces using Sensor Set III

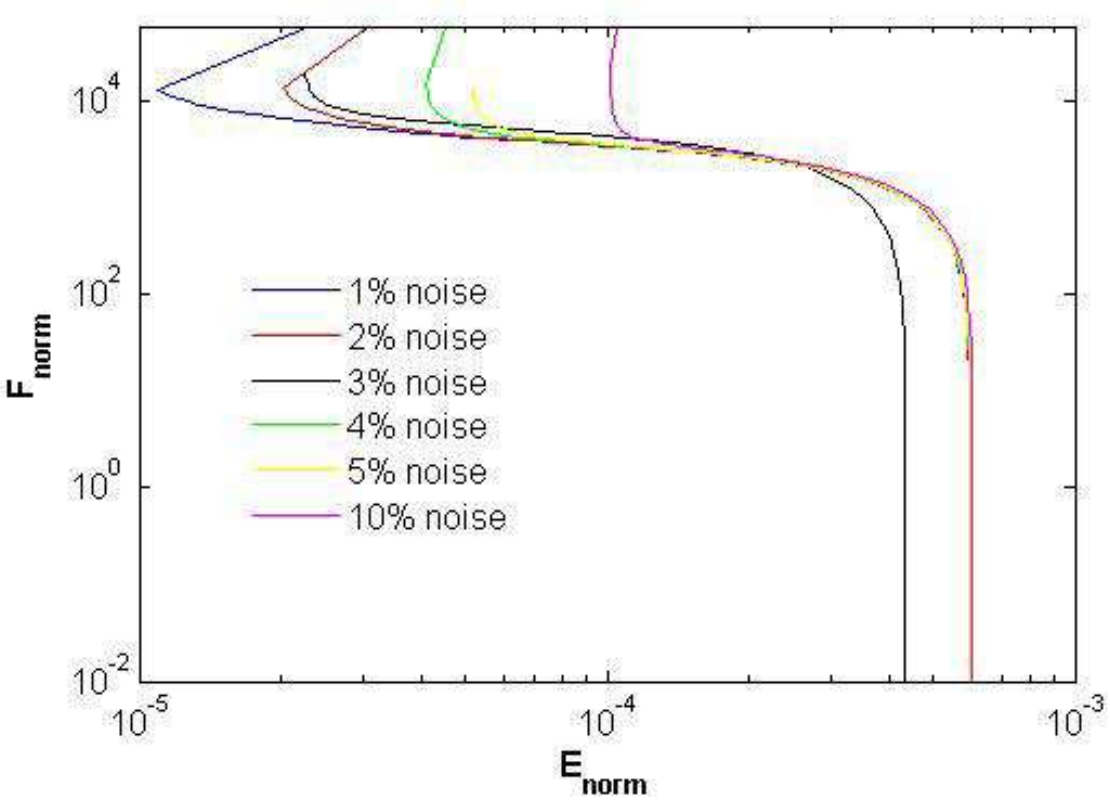

Figure 6.30 – L curves for all noise levels for sensor set II

6.5.7 Effect of Axle Spacing

The effect of the axle spacing on the accuracy of the moving force identification algorithm is analysed for the scenario of a vehicle travelling at 20 m/s subject to the moving forces defined in equation (6.31). The sampling frequency is .0005 s, and 25 modes of vibration are used in the inverse analysis. The four sensor sets contaminated with 3% Gaussian noise are used as the 'measured' input and the axle spacing is varied from 1m to 10m in increments of 1. Figure 6.31 shows the percentage errors in the predicted axle forces versus the distance between the forces.

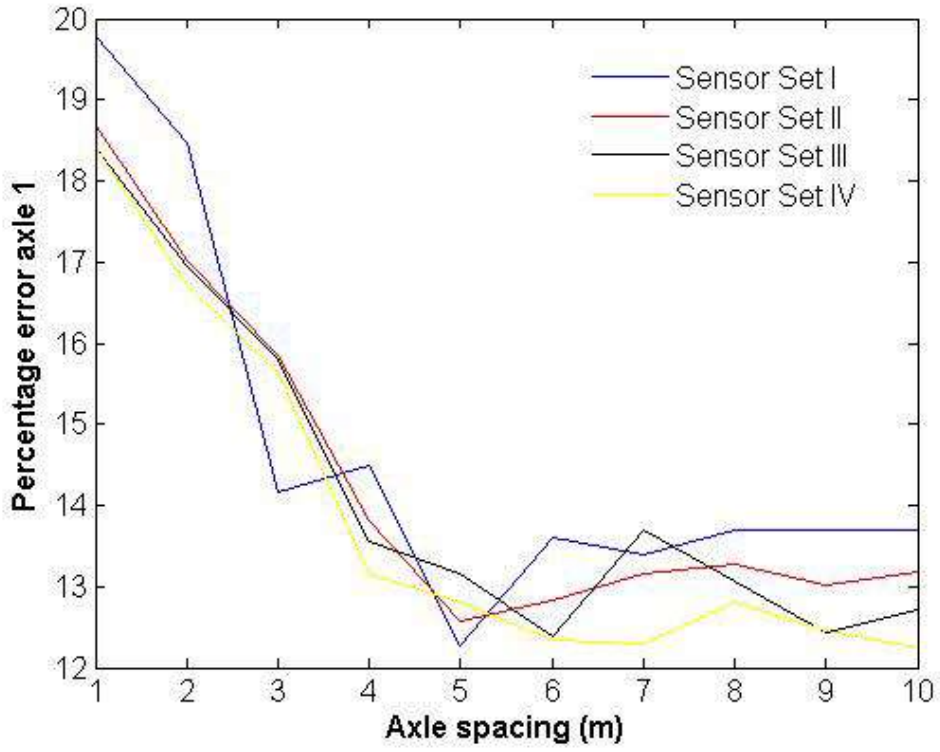

(a) - Axle 1

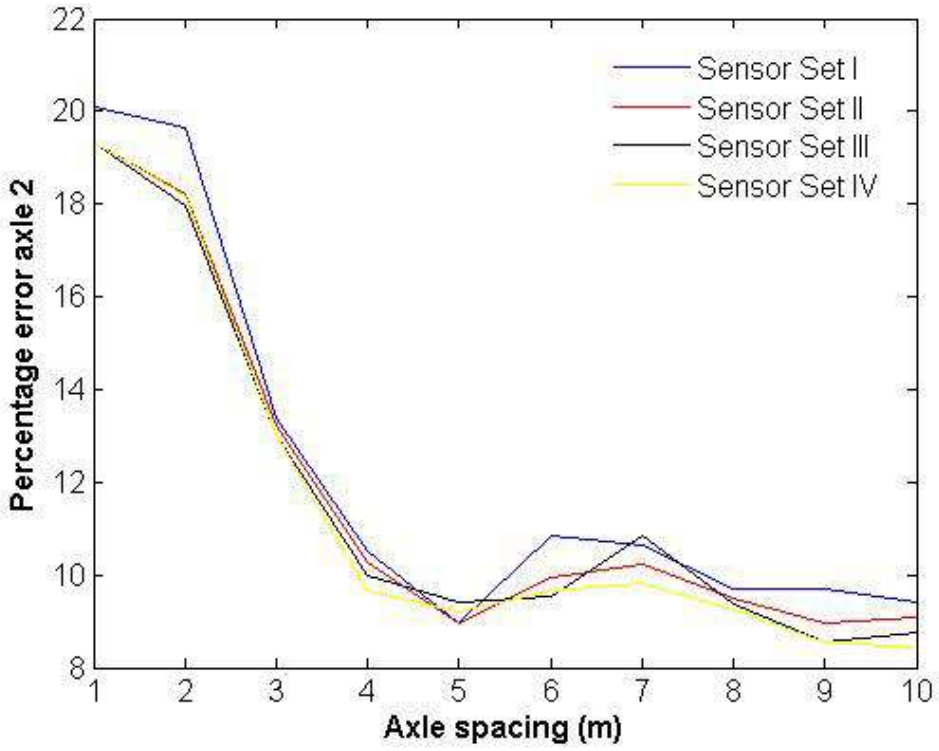

(b) – Axle 2

Figure 6.31 - Percentage error in the identified forces versus the axle spacing

The moving force identification algorithm achieves acceptable result for axle spacing greater than or equal to 3 m, for axle spacing less than this the algorithm cannot accurately distinguish between forces. However it should be pointed out that this error is specific to the particular scenario used in the error analysis, and the particular mesh employed in the inverse model.

6.6 Conclusions

A method to reduce the computational time of the moving force identification algorithm has been developed and numerically validated. The eigenvalue reduction technique has been applied to a two span continuous bridge to validate the proposed method. The assumption that the force can be regularised as if it were at a node, whether or not it is actually at a node, has been replaced with a more exact solution that the force is distributed to the degrees of freedom of the particular element that the force is acting on. It has been shown that for the Fryba vehicle bridge interaction model that the eigenvalue reduction technique coupled, with the new assumption of the nature of the force, results in significant improvement over the algorithm developed in chapter 4. It should also be noted that predicted moving forces on the two-span continuous bridge could be improved if the forces were distributed to the dof's as a product of the shape functions.

An error analysis has been performed to assess the sensitivity of the modified moving force identification algorithm to various parameters. The findings of this analysis results in some recommendations for the implementation of the moving force identification algorithm. The number of modes used in the inverse analysis should be between 20 & 25, and the minimum sampling frequency should be greater than or equal to 1000Hz. The speed of the vehicle can also affect the accuracy of the algorithm; however this accuracy is specific to the combination of sensors used in the inverse analysis. Hence for the overall performance of the MFI algorithm, optimal sensor location is a decision that requires further research.